JOURNAL OF
PETROLOGY

Journal of Petrology, 2017, Vol. 58, No. 7, 1333–1362
doi: 10.1093/petrology/egx056
Advance Access Publication Date: 10 October 2017
Original Article

OXFORD

Enhancing Maficity of Granitic Magma during Anatexis: Entrainment of Infertile Mafic Lithologies

B. B. Carvalho[1]*, E. W. Sawyer[1] and V. A. Janasi[2]

[1]Département des Sciences Appliquées, Université du Québec à Chicoutimi, 555 Boulevard de l'Université, Chicoutimi, QC G7H 2B1, Canada; [2]Instituto de Geociências, Universidade de São Paulo, Rua do Lago 562, CEP 05508-080, São Paulo, SP, Brazil

*Corresponding author. Present address: Dipartimento di Geoscienze, Università degli studi di Padova, Via Gradenigo 6, 35131 Padova, Italy. Telephone: +39(327)3088620. E-mail: bruna.borges-carvalho1@uqac.ca

Received September 1, 2016; Accepted August 22, 2017

ABSTRACT

Most studies of migmatites examine how anatexis occurred in the most fertile units and what happened to that melt, whereas the associated minor lithologies are typically ignored. The Kinawa migmatite in the southern São Francisco Craton of Brazil is the product of water-fluxed melting of a leucogranodiorite that contained dykes of amphibolite. The migmatite consists mostly of pink diatexites, metatexites and leucosomes, but it also contains schollen of amphibolite. This study examines the behaviour of these minor mafic rocks during anatexis to determine what role they play in the formation of migmatites and development of granitic magmas in their source region.The amphibolites are massive or banded Hbl + Pl, and rarely Hbl + Pl + Cpx, schollen in the diatexite migmatite. The amphibolite schollen melted very little, and show a complex morphology suggesting mechanical and chemical interaction with the enclosing leucocratic pink diatexite migmatite. Diatexites and leucosomes immediately adjacent to the schollen have a considerably higher proportion of amphibole (up to 12%) and/or biotite (up to 10%) compared with the diatexite a few tens of centimeters farther away. Six stages of disaggregation and interaction of mafic schollen with the enclosing diatexite magma are recognized: (1) amphibolite layers break up to form schollen, but are mineralogically and texturally unchanged; (2) melt infiltrates into fractures and foliation in the schollen; (3) schollen disaggregate into swarms of single amphibole crystals within the diatexites; (4) amphibole is partially replaced by biotite; (5) flow of the enclosing diatexite magma arranges the detached amphibole crystals into schlieren and aggregates of biotite; (6) detached crystals are completely replaced by biotite and dispersed by magmatic flow to produce a mesocratic to melanocratic homogeneous diatexite. Geochemical modelling indicates that the composition of the diatexites and leucosomes is changed by the wholesale entrainment of the disaggregated mafic schollen or in some cases by the preferential entrainment of detached hornblende or plagioclase crystals. This contamination increases the maficity of initially felsic, leucodiatexite magma, by the addition of FeO + MgO, CaO and TiO_2 (which results in a concomitant decrease in SiO_2), to become a mesocratic to melanocratic diatexite magma that is comparable with typical I-type granites found around the world. Entrainment of mafic material and hornblende in particular strongly influences the behaviour of the rare earth elements, lowering La_N/Yb_N ratios. Thus, non-protolith mafic lithologies within migmatites represent a source of contamination for anatectic melts that results in a significant increase in maficity.

Key words: anatexis; diatexite; entrainment; granitic magma; schollen disaggregation

INTRODUCTION

High-grade metamorphic terrains show that deep levels of the continental crust are reworked by partial melting and deformation-driven melt segregation (Vielzeuf *et al.*, 1990; Sawyer *et al.*, 2011) and are mostly migmatite. The formation of migmatites depends not only on the temperature, pressure and $a_{(H2O)}$ but also on the bulk-rock composition. However, the principal requirement is that there is enough heat to raise a significant volume of rock to temperatures above its solidus.

Fertility is a relative term that describes the propensity of a rock to produce melt (Clemens, 2006). Fertile rocks melt at the imposed *P*–*T* conditions; a more fertile rock produces more melt than a less fertile one, whereas an infertile rock does not melt, although it might at higher temperature. The fertile rocks partially melt and became the neosome; the infertile ones do not and become the paleosome in the resulting migmatite (Sawyer, 2008).

Most studies of partial melting have concentrated on the neosome generated from the most fertile rocks in the migmatite, such as those derived from metapelite, or metagreywacke. The less fertile and infertile rocks that melted a little, or not at all, are generally ignored. Yet the presence of these less fertile rock types appears to play a significant role in the development of migmatites. For example, Skjerlie *et al.* (1993) showed that bulk compositions that produce small amounts of melt on their own may be much more fertile when interlayered with other lithologies that have components that destabilize hydrous phases. Recently, Ganzhorn *et al.* (2016) showed that the stronger, relatively infertile layers in a partially molten heterogeneous gneiss strongly influence the distribution of melt and enhance its segregation and flow during coaxial deformation. Therefore, lithological heterogeneity positively influences the formation of migmatites.

Most granites are produced during partial melting of the lower and middle continental crust (Clemens *et al.*, 2010). However, the compositions of glasses produced in quenched melting experiments using typical crustal rocks (e.g. Patiño Douce & Johnston, 1991; Patiño Douce & Harris, 1998; Acosta-Vigil *et al.*, 2006) are too felsic and have FeO + MgO contents far lower than those of most granites (Chappell *et al.*, 1987; Montel & Vielzeuf, 1997; Stevens *et al.*, 2007). Thus, it has been widely proposed that it is the entrainment of crystals into anatectic melt at the place where melting and segregation occurred that produces a more mafic granitic magma from which the typically mesocratic and melanocratic granites found higher in the crust are derived. The 'restite unmixing' model of White & Chappell (1977) and Chappell *et al.* (1987) argues that the solid (restite) and melt fractions separate, or unmix, to various degrees at the site of melting, and that this process is generally incomplete. The 'restite unmixing' model identifies the phases involved variously as the ferromagnesian minerals (garnet, cordierite, pyroxene, biotite), plagioclase, quartz, zircon and apatite, but makes no distinction as to whether they were peritectic, excess or refractory phases. Other researchers have argued that the geochemical features of S-type granites result from the preferential entrainment of peritectic phases, notably garnet (Stevens *et al.*, 2007; Villaros *et al.*, 2009; Taylor & Stevens, 2010). However, examination of the early stages of melt segregation (Sawyer, 2014), the composition of included phases (Carvalho *et al.*, 2016) and the bulk composition of I-type granites (Clemens *et al.*, 2010) suggests that all the phases in the source rock are entrained as the melt is segregated, not just the peritectic phases; this amounts to a return to the 'restite unmixing' model. Both models apply to the fertile, most melted rocks; no consideration has been given in the literature to the contribution that less melted and non-melted lithologies in the source might make in providing the components, especially via ferromagnesian minerals, essential to making a mesocratic or melanocratic granite magma.

This contribution is focused on the minor mafic rocks in the Kinawa migmatite, part of a reworked Archean tonalite–trondhjemite–granodiorite (TTG) terrane in the southern São Francisco Craton, Brazil. We use detailed field and microstructural information together with bulk-rock and mineral compositions to evaluate (1) how the minor mafic, non-protolith lithologies behaved as their granodiorite host underwent partial melting and magma flow, (2) what textural and compositional consequences arise from the interaction of these mafic rocks and partially melted host granodiorite in the overall migmatite, and (3) what are the implications of these interactions for the formation of granitic magmas in the continental crust.

GEOLOGICAL BACKGROUND

Regional geology

The São Francisco Craton (SFC) is a Precambrian shield (De Almeida, 1977; Alkimin & Marshak, 1998) within the South American continent. It consists of Mesoarchean granite–greenstone terranes reworked during the Neoarchean and Paleoproterozoic (Teixeira & Figueiredo, 1991; Teixeira *et al.*, 1996, 1998; Carneiro *et al.*, 1998).

The Kinawa migmatite occurs within the Cláudio Shear Zone (CSZ in Fig. 1), a significant regional structure that Campos *et al.* (2003) identified as having dextral displacement. This migmatite occurs within the granite–gneiss terrane of the Campo Belo Metamorphic Complex (CBMC) located in the southern portion of the SFC. Much of the CBMC consists of TTG gneisses metamorphosed mainly at amphibolite facies; however, granulite-facies rocks have been described from a few localities (Campos *et al.*, 2003).

Four main periods of magmatism and crustal reworking are recorded in the southern SFC (Lana *et al.*, 2013; Romano *et al.*, 2013; Farina *et al.*, 2015). The

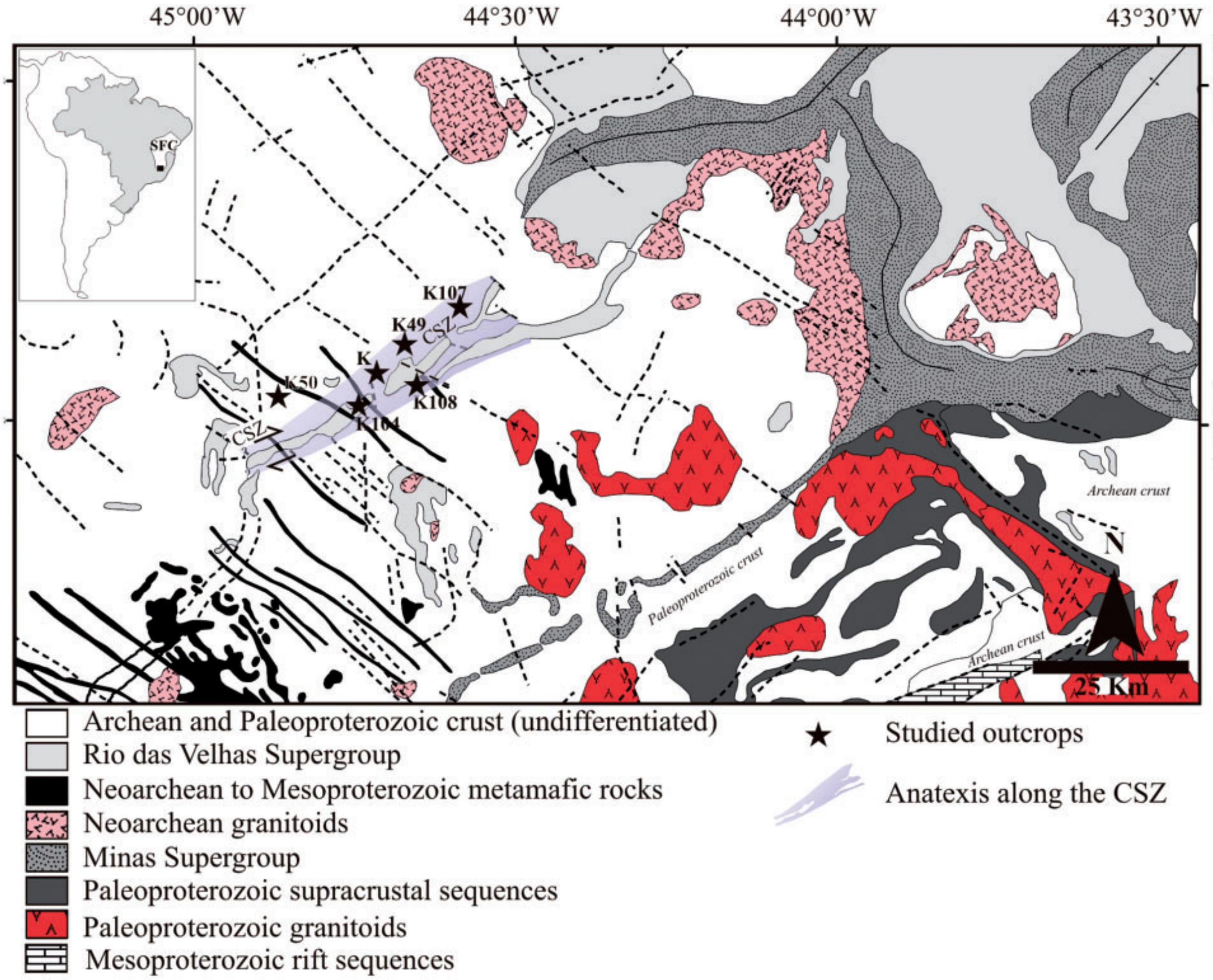

Fig. 1. Geological map showing the location of the outcrops examined in the southern São Francisco Craton, Brazil. K, Kinawa Quarry; CSZ, Cláudio Shear Zone.

oldest, termed the Santa Barbara event (3212–3210 Ma), represents the formation of Mesoarchean TTG crust. The second (2930–2900 Ma), called Rio das Velhas I by Lana *et al.* (2013), is characterized by crustal growth involving the emplacement of granitic magmas and the tectonic accretion of mafic–ultramafic greenstone belt terranes. The third (2800–2760 Ma), called Rio das Velhas II, consists of a regional metamorphic event, and the youngest (2750–2680 Ma) was recently named the Mamona event (Farina *et al.*, 2015) and involved continental convergence and voluminous coeval potassic magmatism (Romano *et al.*, 2013).

Neoarchean supracrustal sequences near the Kinawa migmatite comprise ultramafic rocks, amphibolites, garnet–sillimanite schists and quartzites, and banded iron formations (Oliveira & Carneiro, 2001), and are correlated with the Rio das Velhas Supergroup (Dorr, 1969; Baltazar & Zucchetti, 2007). Younger mafic bodies (gabbros, gabbronorites and diabases) occur throughout the region, typically as NW–SE dykes (Fig. 1).

A late Paleoproterozoic event (2·2–1·9 Ga) is recognized in some parts of the SFC (e.g. Noce *et al.*, 1998, 2000; Teixeira *et al.*, 2015) and represents a very significant period of crustal growth for the South American continent (Teixeira & Figueiredo, 1991). In the southern SFC, this event, renamed the Minas accretionary orogeny by Teixeira *et al.* (2015), is related to the formation of the Mineiro Belt (Ávila *et al.*, 2014).

The Kinawa migmatite

The protolith for the Kinawa migmatite is a leucogranodiorite gneiss, part of typical Archean TTG crust formed at 2·7 Ga (Carvalho *et al.*, 2016). U–Pb (sensitive high-resolution ion microprobe; SHRIMP) dating (Carvalho *et al.*, 2017) of zircon from leucosomes in the Kinawa migmatite indicates that anatexis along the Cláudio shear zone (Fig. 1) occurred at ∼ 2·05 Ga and is therefore coeval with the Minas orogeny, and much younger (>600 Myr) than previously thought (Teixeira *et al.*, 1998).

Carvalho *et al.* (2016) used mineral chemistry and the paragenesis of the main rock types to estimate a maximum temperature of 730°C and pressures between 5·1 and 6·1 kbar for partial melting at Kinawa, which correspond to the upper amphibolite facies. The anatexis of the leucogranodiorite protolith did not involve the breakdown of biotite and was the result of water-present melting via a reaction such as $Pl + Kfs + Qz + H_2O = melt$.

Migmatites at Kinawa are easily recognized because the pre-existing S_1 structures of the protolith have been partially, or completely, overprinted by a steeper syn-anatectic S_2 foliation and structures (e.g. magmatic flow banding and leucosomes) oriented between 308/80 and 124/80, characteristic of the Cláudio Shear Zone. Partial melting was therefore synchronous with strong penetrative deformation in the shear zone. The Kinawa migmatite consists mainly of diatexites and leucosomes, with minor metatexites, grey gneisses, and amphibolites. Diatexite is the most abundant variety of migmatite and is subdivided into three types (Fig. 2a); grey, schlieren, and homogeneous diatexites [see Carvalho *et al.* (2016) for more detail].

Grey diatexites have the smallest grain size, and highest modal plagioclase, quartz, biotite and accessory phases, and are broadly granodiorite in bulk composition. They are enriched in the residual components and correspondingly depleted in the melt component relative to the other diatexites. The schlieren diatexites are the most common variety at Kinawa. They are mostly medium-grained, grey to pinkish rocks with a heterogeneous aspect characterized by portions with variable amounts of biotite-rich schlieren separated by more homogeneous quartzo-feldspathic, formerly melt-rich domains. In contrast, the homogeneous diatexites are coarse-grained pink rocks that range in composition from granodiorite to monzogranite. They have a more felsic aspect owing to a lower modal proportion of biotite, which is generally randomly distributed in the rock. Leucosomes are also abundant at Kinawa and they show a wide range of compositions, from tonalite to alkali-feldspar granite.

Other rocks in the migmatite

Grey gneisses

Grey gneisses are banded mesocratic metatonalites (Fig. 2b) that commonly occur as schollen in the diatexites. Owing to their high biotite content, the S_1 fabric is more strongly developed in these rocks and is a gneissosity. They contain up to 5% K-feldspar and display a fine-grained lepidoblastic metamorphic texture. Some exhibit local evidence for a small degree of partial melting and a retained melt fraction as small leucocratic patches and narrow delicate leucosomes with diffuse margins.

Amphibolites

The leucogranodiorite gneisses outside the Cláudio Shear Zone are considered the likely protolith to the migmatites (Carvalho *et al.*, 2017) and they contain scattered mafic layers interpreted to originate from mafic

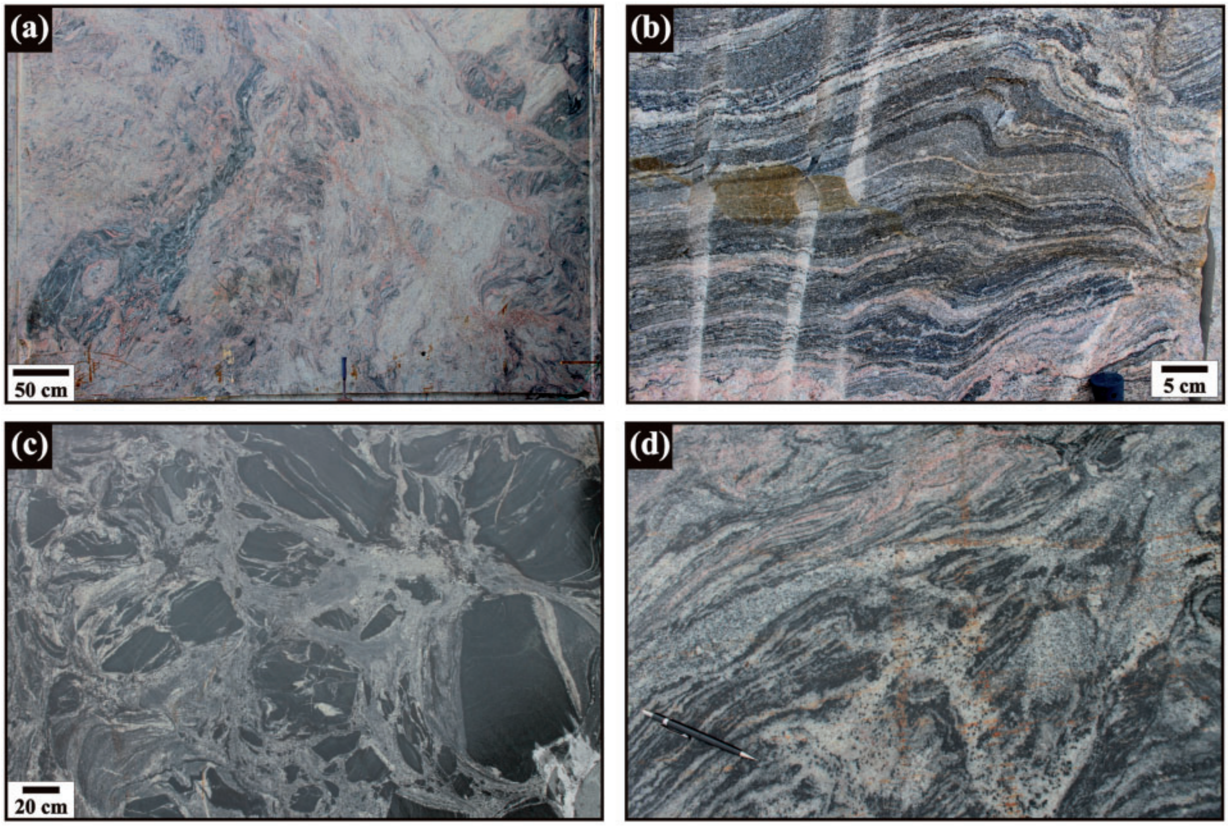

Fig. 2. Macroscopic features of the studied rocks in the field. (a) Typical overall heterogeneous aspect of the Kinawa Migmatite showing schlieren and homogeneous diatexites. (b) Banded grey biotite gneiss with asymmetric folds. (c) Schollen diatexite containing abundant large blocks of amphibolite, which represent resister mafic dykes dismembered during the flow of the diatexite magma around them. (d) Close-up of stromatic metatexite formed by local partial melting.

dykes or sills. These layers have been deformed and metamorphosed; they have the S_1 foliation, locally show boudinage and are amphibolites with the mineral assemblage $Hbl + Pl \pm Cpx$. Similar metamafic rocks also occur within the Kinawa migmatites and are predominantly fine- to medium-grained amphibolites. The S_1 foliation is poorly developed in the thickest layers (>1 m), which have a massive microstructure dominated by coarse, decussate amphibole. However, compositional banding and the S_1 foliation are present in some thinner amphibolites, which also commonly show boudinage. The banding is defined by variation in the modal proportions of plagioclase and amphibole and locally, in the centre of some layers, by pyroxene and plagioclase. In a few places thin amphibolite layers are folded. The amphibolite layers become disrupted and form dark-coloured schollen, or rafts, in the diatexite migmatites (Figs 2c and 3). The amphibolite layers probably represent the competent mafic dykes in the leucogranodiorite protolith that were transposed parallel to the S_1 foliation and subsequently dismembered and recrystallized during the Paleoproterozoic anatectic event that created the Kinawa migmatite. The amphibolite layers do not contain patches of neosome, and the expected peritectic phases (e.g. orthopyroxene, garnet) from hornblende-consuming fluid-absent incongruent melting reactions are absent. Thus, they appear not to have partially melted sufficiently to leave macroscopic evidence of it. Therefore, in the field, the amphibolites are considered to be paleosome, or resister, layers in the migmatite.

Metatexites

Metatexite migmatites are not abundant, but are distinctive because they conserve the S_1 foliation. In contrast to the grey gneisses, metatexites are melanocratic and contain stromatic leucosomes (Fig. 2d) and/or small patches of leucosome located between boudins or in small shear bands. In many metatexites the leucosomes are surrounded by melanosomes.

The melanosomes exhibit a medium-grained lepidoblastic texture and are mainly composed of plagioclase (45–50%), brown biotite (up to 30%), and quartz (20%). Anhedral hornblende (up to 3%) occurs within aggregates of biotite; thus, initially some melanosomes may have had more hornblende, which was later replaced by biotite as the melt in the leucosome crystallized. Plagioclase is anhedral and some grains have corroded shapes (Fig. 4a). Similarly, some biotite grains have irregular outlines (Fig. 4a) indicating that biotite may have been a reactant phase with plagioclase and quartz to produce melt (e.g. $Pl + Qtz + Bt + H_2O = melt + Ttn$). K-feldspar occurs as rare (up to 2%) interstitial films along the junctions between corroded plagioclase and biotite (Fig. 4a), and is interpreted to pseudomorph former melt.

The accessory phases (Fig. 4a and b) in the melanosome are apatite (0·5–0·7%), allanite (0·2–1·1%), titanite (~0·3–1·8%), ilmenite (0·5–1%), zircon (0·1–0·5%) and rarely rutile. Some samples have remarkably high contents of accessory phases (e.g. K75) suggesting that melanosomes could be sites where incompatible elements, such as P, Ti, Zr and rare earth elements (REE) were concentrated.

METHODS

Major element contents of plagioclase, K-feldspar, pyroxene, amphibole and biotite from 16 samples were obtained by electron microprobe (see Table 1 and complete dataset in Supplementary Data Electronic Appendix Table 1; supplementary data are available for downloading at http://www.petrology.oxfordjournals.org). The concentration of trace elements in plagioclase, K-feldspar, pyroxene, amphibole and biotite was determined by laser ablation quadrupole inductively coupled plasma mass spectrometry (LA-Q-ICP-MS) on four representative samples (see Table 3 and complete dataset in Supplementary Data Electronic Appendix Table 2). A subset of 19 samples was selected for whole-rock analysis of major and trace elements by X-ray fluorescence (XRF) and ICP-MS (see Table 4).

A detailed account of all the analytical procedures is given in the Supplementary Data Electronic Appendix, Analytical Methods.

MICROSTRUCTURE AND MAJOR ELEMENT MINERAL COMPOSITIONS

Interaction between diatexite and schollen

Throughout the Kinawa migmatite, diatexites display magmatic flow structures and contain abundant leucosomes (Carvalho *et al.*, 2016), which indicate that they were melt-rich rocks (i.e. the diatexite was a magma). The diatexites also contain abundant fragments, mostly rounded, but some angular (Figs 2c and 3), of amphibolite as schollen. In most places there is strong evidence for both mechanical and chemical interaction between the host diatexite magma and the mafic schollen. Typically the diatexite close to (<30 cm) a mafic scholle contains a higher proportion of ferromagnesian minerals (hornblende and/or biotite) and has a different colour from that farther away (>1 m; diatexites are usually pink, but when around the schollen they are white; see Fig. 3a–c). Examination of many schollen indicates that some are modified more than others; this suggests that there is a progression in the extent to which and the manner in which the mafic schollen and enclosing melt-rich migmatite have interacted (see summary of stages in Table 2).

Unmodified mafic schollen

At the outcrop the least modified mafic rocks are generally banded, with different proportions of clinopyroxene, hornblende and plagioclase from band to band. Layers in the centres of some of the largest (~1 m)

Table 1: Representative microprobe analyses of plagioclase, K-feldspar, biotite and amphibole from the Kinawa migmatite

Sample	Unit	Analysis	wt %													
			SiO_2	TiO_2	Al_2O_3	FeO	Cr_2O_3	MnO	NiO	MgO	CaO	Na_2O		Total		
Cpx																
K22a	HD	Px4	50·52	0·05	3·17	9·3	0·11	0·7	0·02	11·53	23·16	0·47		99		
K24	A	Px1	52·28	0·16	1·16	10·6	0·09	0·46		11·6	23·62	0·42		100·4		
			SiO_2	TiO_2	Al_2O_3	FeO	MnO	MgO	CaO	Na_2O	K_2O	F	Cl	Total		
Bt																
K93a	HL	Bt15	35·37	3·89	15·38	24·16	0·28	7·27	0·02	0·06	9·37	0·39	0·07	96·2		
K20a	M	Bt17	35·49	2·92	15·5	22·67	0·3	8·5	0·04	0·11	9·36	0·48	0·1	97		
K5a	A	Bt3	36·46	1·93	15·81	19·36	0·3	11·99	0·01	0·12	9·61	0·54	0·05	96·3		
K22b	HD	Bt21	36·34	2·84	14·99	21·62	0·32	9·4	0·01	0·09	9·39	0·61	0·07	95·7		
			SiO_2	TiO_2	Al_2O_3	FeO	MnO	MgO	CaO	Na_2O	K_2O	F	Cl	Total		
Amp																
K24	A	Am8	42·17	1·34	11·28	17·71	0·34	9·58	12·1	1·26	1·49	0·3	0·04	97·6		
K5a	HD	Am3	42·85	1·08	9·42	18·26	0·52	10·51	11·8	1·3	1·06	0·18	0·06	97		
K89	HL	Am7	41·81	1·67	10·33	22·1	0·65	7·33	11·2	1·47	1·34	0·2	0·08	98·2		
K20a	M	Am1	40·24	1·33	10·58	22·21	0·53	7·31	11·54	1·3	1·32	0·12	0·08	96·5		
			SiO_2	TiO_2	Al_2O_3	FeO	MnO	MgO	CaO	Na_2O	K_2O	SrO		Total		
Plag																
K24	A	Pl27	57·4	0	27·17	0·13	0	0	9·05	6·49	0·19	0·07		100·5		
B2	HD	Pl55	62·49	0	23·91	0·11	0·04	0·01	5·15	8·53	0·36	0		100·7		
K22b	HD	Pl34	61·25	0	24·4	0·16	0	0·01	5·63	8·23	0·23	0·13		100·03		
K20d	HL	Pl48	61·64	0	24·07	0·15	0	0·01	5·31	8·39	0·23	0·07		99·9		
			SiO_2	TiO_2	Al_2O_3	FeO	MnO	MgO	BaO	CaO	Na_2O	K_2O		Total		
Kfs																
K89	HL	Kf4	64·39	0	17·87	0·03	0	0·01	0·45	0·02	0·43	16·27		99·5		
K20d	HL	Kf34	64·21	0	18·48	0·16	0	0·02	0·32	0·03	0·35	15·77		99·3		
	a.p.f.u.															*X*Mg
	Si	Al	Ti	Fe^{2+}	Mg	Mn	Ca	Na					Wo	En	Fs	
Cpx																
K22a	1·91	0·14		0·29	0·65	0·02	0·94	0·03					49·3	34·1	16·6	0·69
K24	1·96	0·05	0·01	0·33	0·65	0·02	0·95	0·03					48·8	33·3	17·9	0·66
	Si	Al	Ti	Fe^{2+}	Mn	Mg	Ca	Na	K	F	Cl					*X*Mg
Bt																
K93a	5·55	2·84	0·46	3·17	0·04	1·7	0	0·02	1·88	0·39	0·04					0·35
K20a	5·59	2·88	0·35	2·99	0·04	2	0·01	0·03	1·88	0·48	0·05					0·4
K5a	5·6	2·86	0·22	2·49	0·04	2·74	0	0·04	1·88	0·52	0·03					0·52
K22b	5·68	2·76	0·33	2·83	0·04	2·19	0	0·03	1·87	0·61	0·04					0·44
	Si	Al	Fe^{3+}	Ti	Mg	Fe2	Mn	Ca	Na	K	Cl	F				*X*Mg
Amp																
K24	6·38	2·01	0·33	0·15	2·16	1·91	0·04	1·96	0·37	0·29	0·01	0·15				0·53
K5a	6·46	1·67	0·75	0·12	2·36	1·55	0·07	1·91	0·38	0·2	0·01	0·09				0·6
K89	6·38	1·86	0·64	0·19	1·67	2·18	0·08	1·83	0·43	0·26	0·02	0·1				0·43
K20a	6·26	1·94	0·74	0·16	1·69	2·15	0·07	1·92	0·39	0·26	0·02	0·06				0·44
	Si	Al	Fe^{2+}	Mn	Mg	Ca	Na	K					Ab	An	Or	
Plag																
K24	5·14	2·86	0·01	0	0	0·87	1·13	0·02					55·9	43	1·1	
B2	5·52	2·49	0·01	0	0	0·49	1·46	0·04					73·5	24·5	2	
K22b	5·45	2·56	0·01	0	0	0·54	1·42	0·03					71·6	27·1	1·3	
K20d	5·48	2·52	0·01	0	0	0·51	1·45	0·03					73·1	25·6	1·3	
	Si	Al	Fe^{2+}	Mn	Mg	Ba	Ca	Na	K				Ab	An	Or	
Kfs																
K89	6·03	1·97	0	0	0	0·02	0	0·08	1·94				3·9	0·1	96	
K20d	5·98	2·03	0·01	0	0	0·01	0	0·06	1·87				3·3	0·2	96·6	

Atoms per formula unit were calculated using 8 oxygens for feldspar, 22 oxygens for biotite, and 23 oxygens for amphibole. Full dataset is given in Supplementary Data Electronic Appendix Table 1. Cpx, clinopyroxene; Bt, biotite; Amp, amphibole; Plag, plagioclase; Kfs, K-feldspar; HD, Hbl-diatexite; A, amphibolite; HL, Hbl-leucosome, M, melanosome.

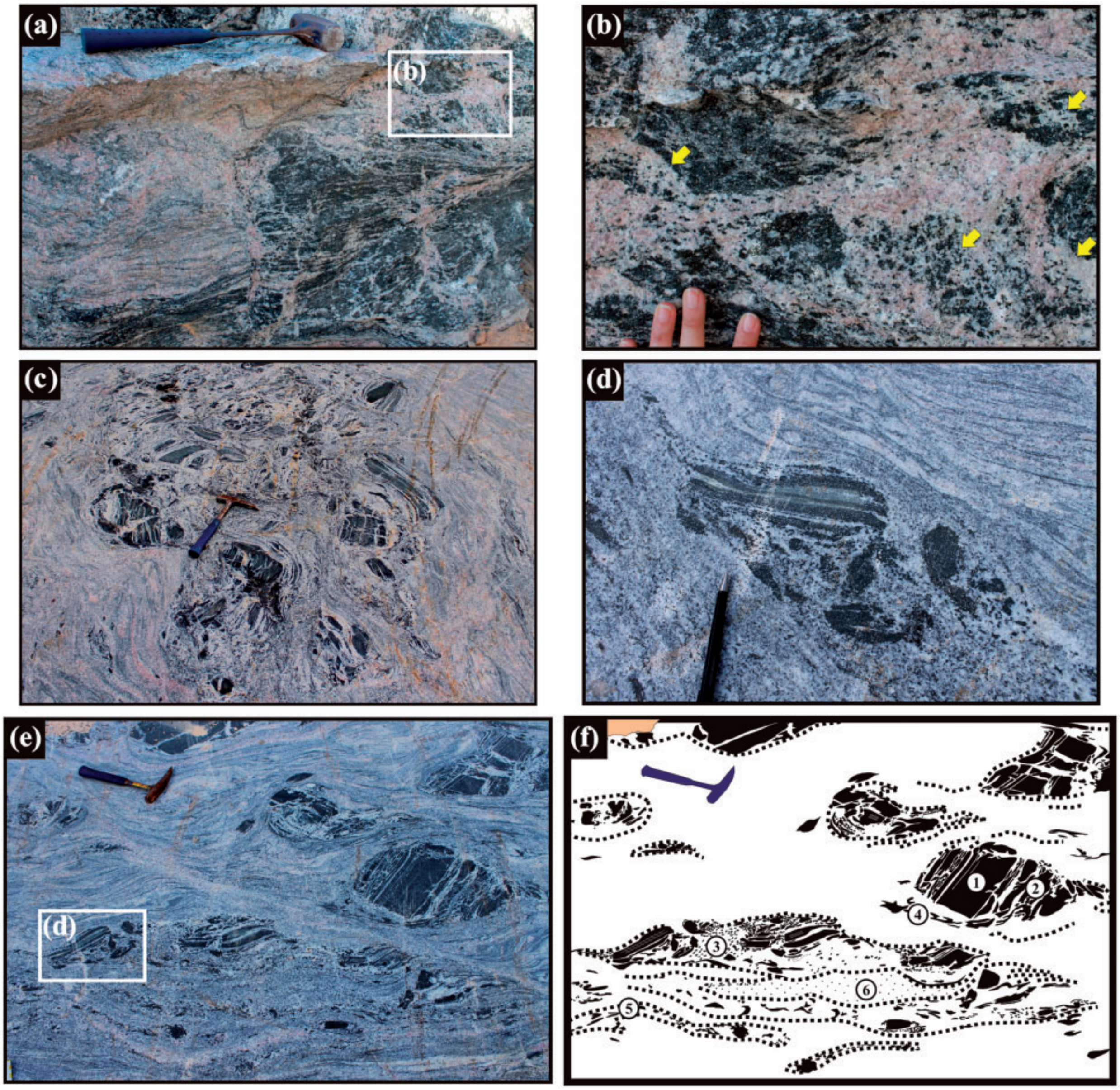

Fig. 3. (a) Leucosome invading a mafic scholle and dividing it into smaller fragments. The leucosomes appear to root in the diatexite, which suggests that melt from the diatexite penetrated into the amphibolite (Stage 2) and initiated its disaggregation (Stage 3). (b) Close-up of (a) showing different composition of leucosome at the contact with amphibolite. Local disaggregation of the scholle releases swarms of hornblende crystals into the diatexite, and in these places the diatexite is no longer pinkish but is white (see yellow arrows), indicating chemical reaction between solid fragments and the diatexite magma. (c) More advanced stage in the disruption of schollen, also showing contamination of the host pink diatexite around the schollen. It should be noted that the leucocratic material close to the diatexite is white and contains crystals of hornblende, whereas it is pink farther away. (d) Close-up showing the erosion of a fragmented scholle and formation of a tail leading to schlieren formation. (e) Pink schlieren diatexite containing numerous rounded schollen with augen-like shapes that indicate flow of the diatexite magma around them. The diatexite in the lower half has a high proportion of entrained hornblende. (f) Sketch of (e) emphasizing the principal features of the disaggregation of schollen. (1) Mafic scholle as coherent fragments in the diatexite. (2) Fractured schollen as a result of infiltration of melt. (3) Swarm of amphibole crystals formed by the disaggregation of smaller blocks during flow of the host diatexite. (4) Short wide amphibole-rich schlieren parallel to the edges of a scholle. (5) Long thin biotite-rich schlieren with little amphibole. (6) Dispersion of the detached crystals producing a mesocratic and homogeneous enclosing diatexite.

schollen have a granular well re-equilibrated metamorphic microstructure (Fig. 4c), with ~35 modal % light green diopside ($X_{Mg} \sim 0{\cdot}63$–$0{\cdot}66$), ~35% plagioclase ($An_{37–45}$) and ~20% dark green hornblende ($X_{Mg} \sim 0{\cdot}44$–$0{\cdot}54$). The crystals do not exhibit compositional zoning. The accessory phases are titanite (2%), magnetite (4%) and apatite (~1%). More commonly the amphibolites have recrystallized to a coarse-grained decussate metamorphic microstructure composed of 55–60% pargasite ($X_{Mg} \sim 0{\cdot}45$–$0{\cdot}6$), which contains relict diopside (up to 15%) in its core (Fig. 4d), and ~25% slightly more sodic plagioclase ($An_{27–40}$). Thus, mineral compositions change from the core to the margins of the schollen. The accessory phases are mainly apatite,

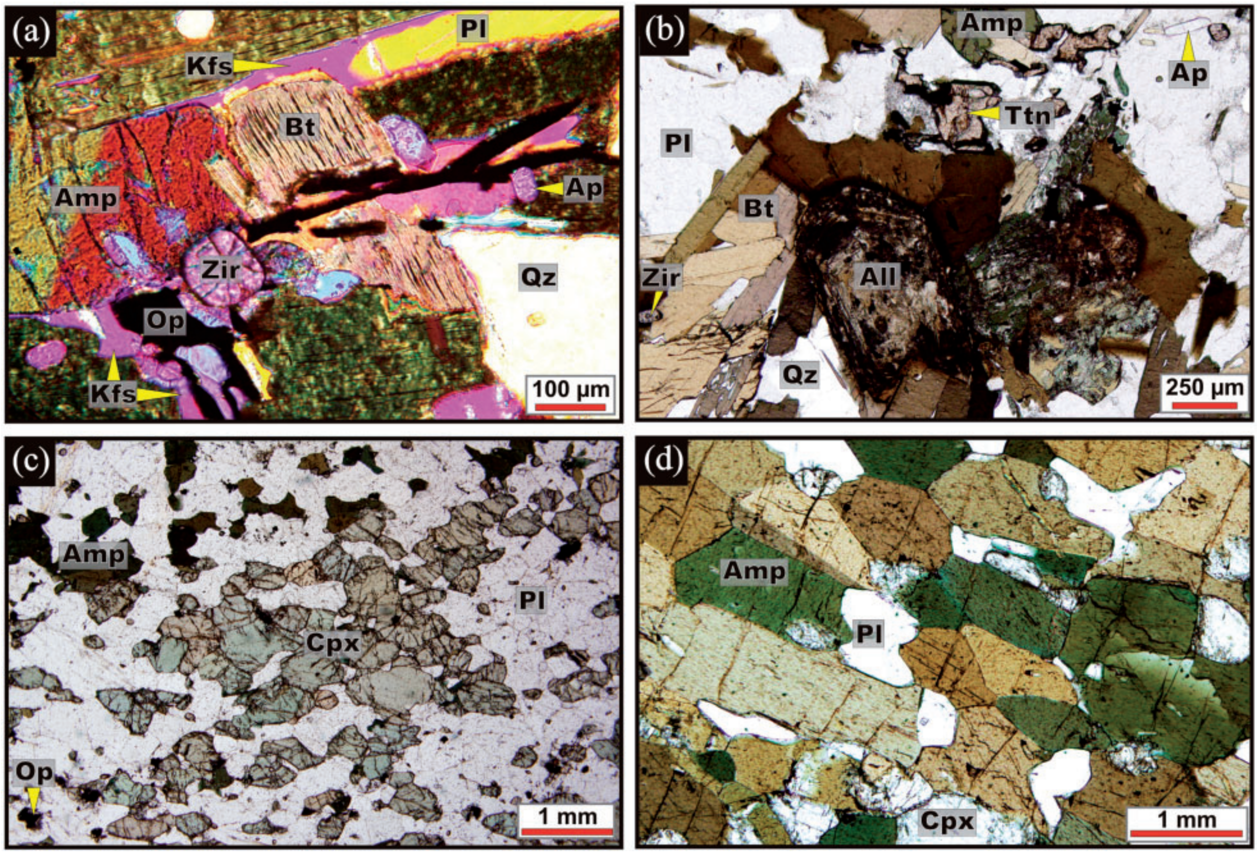

Fig. 4. Photomicrographs of the microstructures in schollen. (a) Metatexite scholle showing a narrow mineral film of K-feldspar between corroded plagioclase and biotite interpreted as microstructural evidence for partial melting. The abundance of accessory minerals in this residual rock should be noted. (b) Melanosome with high modal proportions of allanite, titanite, zircon and apatite. (c) Light green diopside, locally replaced by dark green hornblende (upper left), plagioclase and ilmenite forming a granular texture in the core of an amphibolite scholle. (d) Amphibolite scholle with a mineral assemblage containing hornblende with cores of diopside and plagioclase. This well-equilibrated microstructure indicates upper amphibolite-facies metamorphic conditions. Kfs, K-feldspar; Bt, biotite; Qz, quartz; Pl, plagioclase; Amp, amphibole; Op, opaque minerals; Zir, zircon; Ap, apatite; All, allanite; Ttn, titanite; Cpx, clinopyroxene.

magnetite, titanite, quartz, and rarely carbonate. The microstructure and extent to which clinopyroxene is replaced by amphibole appear to correlate with the size of schollen; the smaller ones are dominated by large decussate hornblende and plagioclase. The amphibole–plagioclase geothermometer of Holland & Blundy (1994) yields two different temperatures (calculated at 5 kbar) from the amphibolites: 828°C from the Cpx + Hbl + Pl core and 773°C for Hbl + Pl margin. At such temperatures the studied rocks could have undergone fluid-absent melting; however, there is no evidence for that. In the literature, other researchers (e.g. Campos *et al.*, 2003) have shown that some regional rocks reached granulite-facies conditions during the Archean. Thus, we interpreted these temperatures as recording an Archean metamorphism and not the Paleoproterozoic anatexis.

Stage 1: mafic schollen as coherent fragments in the diatexite

In Stage 1 the schollen of amphibolite are discrete blocks within the diatexite and range in size from tens to just a few centimetres (Figs 2c and 3). They are mainly composed of ~50 modal % dark green pargasite (X_{Mg} 0·45–0·6), which in rare cases contains minor amounts (~3%) of diopside ($Wo_{47-49}En_{29-35}$; X_{Mg} 0·59–0·69) in its core, ~35% plagioclase (An_{22-40}) and ~10% quartz. Again at this stage, the crystals do not exhibit significant zoning; all the compositional variations are between grains and are related to position within the schollen (e.g. centre to margin) and the stage of modification. The accessory phases (<1%) are apatite, titanite, ilmenite and carbonate. The microstructure (Fig. 5a) in these schollen is well equilibrated and comparable with that in the largest unaltered amphibolite schollen (Fig. 4d).

Thin quartzo-feldspathic films (<20 μm), which contain K-feldspar (Or_{91-97}), outline the boundaries between adjacent hornblende crystals at the periphery of some schollen. These films can be interpreted as evidence either of local partial melting of the quartzo-feldspathic domains between hornblende crystals in the amphibolites, or of melt from the host diatexite that has infiltrated along grain boundaries (Fig. 3a, b and d). In some schollen, the rims of hornblende crystals in contact with the quartzo-feldspathic films show minor (<1%) replacement by biotite (X_{Mg} 0·51–0·59). Applying

Table 2: Summary description of microstructural stages during the interaction of the melt and amphibolite schollen

Stage 1	Mafic schollen as coherent fragments in the diatexite
Stage 2	Infiltration of melt and modification of blocks
Stage 3	Disaggregation of blocks and formation of swarms of hornblende crystals
Stage 4	Hornblende is partially replaced by biotite
Stage 5	Aggregates of biotite and formation of schlieren
Stage 6	Dispersion

the Holland & Blundy (1994) Amp–Pl geothermometer indicates temperatures up to 758°C at 5 kbar for these schollen.

Stage 2: infiltration of melt and modification of blocks

The next stage, demonstrated by many mafic schollen, is the presence along S_1 foliation planes, the compositional banding and discordant, planar or curvi-planar fractures (Fig. 3a) of pink quartzo-feldspathic material, interpreted to have been melt from the surrounding diatexite. Where there was sufficient melt to form an interconnected network the schollen becomes sufficiently weak that they start to break into smaller, typically angular, fragments (Fig. 3b–f). Rare films of plagioclase ($An_{21–26}$) and K-feldspar ($Or_{94–97}$) between the hornblende crystals may be vestiges of the infiltrated melt, or, alternatively, the films could be the products of local partial melting of the quartzo-feldspathic portions of the schollen.

Stage 3: disaggregation of blocks and formation of swarms of hornblende crystals

The onset of this stage appears to occur when the quartzo-feldspathic mineral films between hornblende crystals are developed in much of the interior of the schollen. These films could be result of local partial melting of the amphibolite. However, in some cases these emanate from melt-filled cracks (see Stage 2) and probably represent sites of infiltration of melt from the surrounding diatexite. This suggests that widespread grain-scale development of melt films between hornblende crystals became sufficient to weaken the schollen so that single crystals became detached and the schollen were able to begin to disaggregate. At this stage it is still possible to recognize that the fragments were derived from formerly much larger schollen (Fig. 3e and f). The detached hornblende forms swarms of crystals randomly distributed within the adjacent diatexite. This diatexite contains 9–15% subhedral hornblende, either as large isolated crystals (Fig. 5b) or as aggregates of crystals, and has a coarse-grained heterogranular texture, in which 30–40% plagioclase ($An_{21–28}$) occurs as euhedral to subhedral crystals with no significant compositional zoning together with 25–30% quartz to form the framework structure in the rock. The interstices of the framework are filled by 5–19 modal % K-feldspar ($Or_{91–97}$). Minor (<1%) replacement of the hornblende by biotite (X_{Mg} 0·51–0·59) occurs locally. At this stage hornblende is the principal mafic mineral in the diatexite. Most of the hornblende grains in the swarms of crystals have major element compositions similar to that of amphibole in Stage 1; they are pargasite with $X_{Mg} \sim 0{\cdot}45–0{\cdot}6$. However, some crystals have higher Si (~6·5–6·65 a.p.f.u.) contents and range in composition from edenite to Fe-edenite. Accessory phases in the contaminated diatexite are apatite, allanite, ilmenite, and titanite. The temperatures derived from the Amp–Pl geothermometer (Holland & Blundy, 1994) range from 711 to 727°C and are comparable with the peak temperatures of anatexis (~730°C) estimated by Carvalho *et al.* (2016).

In most cases the individual hornblende crystals in the swarms do not have a preferred orientation (Fig. 3e and f). This implies the diatexite magma around these schollen became static after the hornblende crystals were shed into it.

Stage 4: hornblende partially replaced by biotite

Hornblende is still present in Stage 4; however, it is mostly replaced by biotite. The replacement occurs as medium-grained plates of biotite at the rims of hornblende, or as fine-grained skeletal intergrowths with quartz forming a symplectite (Fig. 5c). The presence of symplectite suggests that the entrained hornblende has reacted with the anatectic melt in the diatexite to produce biotite + quartz and presumably a modified melt composition.

Locally, hornblende-rich schlieren occur parallel to the boundaries of the schollen; these are wider and shorter than biotite-rich schlieren. The hornblende schlieren also contain plagioclase and quartz and locally biotite, which partially replaces hornblende (Fig. 5e). The presence of hornblende schlieren in some domains, and swarms of randomly distributed crystals in others, suggests that the flow in the diatexite was probably heterogeneous.

In places chlorite replaces hornblende together with opaque minerals and carbonate. This paragenesis is interpreted to be due to retrograde metamorphism.

Stage 5: aggregates of biotite and formation of schlieren

The next stage in the schollen–diatexite interaction can be seen in places where magmatic flow of the host diatexite around the schollen has occurred as the hornblende crystals were shed. The detached crystals are collected into schlieren (Fig. 3d–f). Initially, the schlieren occur as short wide bands with low aspect ratio, and are composed of hornblende and biotite derived from it (Fig. 5e). With increased magmatic strain the schlieren become progressively longer and thinner (i.e. increase in aspect ratio) and biotite entirely replaces hornblende (Fig. 5f). The biotite occurs as large, well-formed dark brown crystals (Fig. 5d) that may contain apatite, titanite or ilmenite (Fig. 5f). The biotite that replaces hornblende

Table 3: Representative trace element analyses of minerals in the Kinawa migmatite (values in ppm)

Mineral:	Plagioclase			CPX	Amphibole					Biotite						
Sample:	K5(K5a)	K5(K5a)	K22 (K22a)	K22 (K22b)	K22A	K22(K22a)	K22(K22a)	K5 (K5a)	K5 (K5b)	K5 (K5a)	K22(K22a)	K22(K22b)	K22(K22b)	K5(K5b)	K5(K5a)	K5(K5b)
Analysis:	B1PL38	B5PL31	K22APL1a	K22BPL14	PX1	K22a-A16	K22a-A2	B1-ANF11	B5-A2a	B1-AM16	K22a-BT1	K22b-BT10	K22b-BT5b	B5-BT17	B1-BT23b	B5-BT14b
Stage:	1	3	1	3	1	1	3	1	3	4	1	3	4	4	4	5
Li	0·05	1·24	0·48	0·08	31·8	3·5	9·63	8·13	10·2	6·31	256·7	223·6	246	254·1	254·5	232·4
Be	3·62	2·99	2·6	3·42	2·47	2·48	4·29	4·8	5·27	3·56	0·37	0·75	0·22	0·46	0·35	0·58
Sc	0·83	0·85	1·28	1	44·4	41·2	269	73·1	139	76·01	25·29	63·9	47·7	35·84	7·46	10·45
Ti	16·9	20·6	27·4	18·9	597	5225	6664	6034	6340	5558	10630	9600	13190	10170	12960	9810
V	b.d.l.	0·108	0·2	b.d.l.	169	288·2	267·1	333·5	310·2	324	221·5	230·8	224·4	304·9	297·9	303·3
Cr	b.d.l.	b.d.l.	b.d.l.	b.d.l.	725	1406	809	412·7	591	433·7	1038	254	272	395	424	556
Co	0·036	0·038	0·122	0·023	41·7	62·7	41·9	48·3	41·2	49·32	63·9	57·2	64·9	63·7	77·9	73
Ni	0·26	0·25	3	0·17	150·2	264·3	62·1	153·7	118·6	97·1	117	102	100	107	146	147
Cu	0·74	0·77	25·2	1·72	0·82	0·65	0·59	0·31	0·31	0·429	6·8	1·26	0·64	0·75	1·2	1·88
Zn	1·94	2·05	26·8	3·22	109·5	156·2	142·5	335	217·4	72·6	194·8	219·9	195·5	201·2	210	205·5
Ga	25·6	30·2	30·2	35·3	6·25	20·62	32·5	26·9	30·11	26·9	114·8	181·8	127·4	79·9	184·7	178·6
Rb	0·31	2·09	1·18	0·25	0·52	4·67	8·28	7·85	5·32	5·9	535	541	586	513	563	495
Sr	444	310	388	323	9·29	10·56	22·22	18·1	16·21	24·1	1·65	1·35	0·81	0·725	0·733	1·6
Y	0·091	0·102	0·073	0·232	21·66	84·2	345·1	206·7	285·5	163·7	0·061	2·27	0·048	0·023	0·034	0·099
Zr	0·114	0·171	0·3	0·12	16·5	37·3	56·2	46·8	50·7	42	0·667	0·35	0·274	0·51	0·171	0·303
Nb	b.d.l.	b.d.l.	b.d.l.	b.d.l.	0·57	28·64	68·1	44·3	44·6	32·71	55·6	10·47	44·2	47·1	47·7	22·4
Cs	b.d.l.	b.d.l.	b.d.l.	b.d.l.	0·03	b.d.l.	b.d.l.	b.d.l.	b.d.l.	b.d.l.	16·11	16·1	17·3	12·18	14·01	12·41
Ba	82·1	66	76·9	91·8	1·36	18·3	34·2	28·4	24·8	23·65	638	852	749	361	838	815
La	3·53	4·44	6·36	4·75	2·65	12·16	25·33	18·4	23·5	18·5	0·066	0·336	0·063	0·0147	0·0132	0·039
Ce	3·9	4·93	8·18	6·57	7·98	43·2	95·9	69·9	97·8	63·1	0·121	1·16	0·105	0·022	0·0027	0·071
Pr	0·27	0·381	0·65	0·475	1·37	6·69	16·53	12·73	17·66	10·47	0·0095	0·156	b.d.l.	0·0032	b.d.l.	0·0087
Nd	1·76	2·16	3·49	2·78	7·5	36·5	93·7	69·9	100	56·2	0·082	0·99	0·04	0·026	b.d.l.	0·054
Sm	0·122	0·105	0·141	0·155	2·51	10·5	43·7	25·9	37·7	20·38	0·074	0·41	0·057	b.d.l.	0·068	0·095
Eu	0·702	0·769	0·98	1·07	0·62	2·31	4·15	3·74	3·58	3·32	0·03	0·065	0·038	0·016	0·054	0·046
Gd	0·04	0·073	0·19	0·136	2·74	12·03	61	33·6	48·6	24·82	0·52	0·86	0·41	0·27	0·503	0·56
Tb	b.d.l.	b.d.l.	0·017	0·012	0·53	2·114	11·73	6·02	8·83	4·76	0·0011	0·08	0·0023	b.d.l.	b.d.l.	b.d.l.
Dy	0·015	b.d.l.	0·02	0·024	3·68	14·16	72·4	38·6	56·5	29·63	0·021	0·46	b.d.l.	0·0015	b.d.l.	b.d.l.
Ho	0·0074	0·0044	0·0099	0·011	0·75	2·9	14·79	7·69	11·22	6·22	b.d.l.	0·097	b.d.l.	b.d.l.	0·0021	0·0105
Er	b.d.l.	0·012	0·019	0·035	2·31	8·55	35·6	21·38	29·91	16·42	b.d.l.	0·17	b.d.l.	b.d.l.	b.d.l.	0·015
Tm	b.d.l.	b.d.l.	0·006	b.d.l.	0·37	1·244	4·46	2·9	3·83	2·335	b.d.l.	0·034	0·0026	b.d.l.	b.d.l.	0·0023
Yb	b.d.l.	0·008	0·006	0·007	2·97	9·93	26·3	26·4	b.d.l.	15·21	0·0025	0·105	b.d.l.	0·015	0·0011	b.d.l.
Lu	b.d.l.	b.d.l.	b.d.l.	0·0057	0·58	1·212	3·32	2·43	3·12	2·079	b.d.l.	0·0092	b.d.l.	0·0024	b.d.l.	0·0035
Hf	0·014	b.d.l.	0·013	0·068	0·85	2·21	3·06	2·63	2·68	2·05	0·054	0·032	0·036	0·085	0·052	0·013
Ta	b.d.l.	b.d.l.	b.d.l.	b.d.l.	0·06	3·56	3·7	2·37	3·16	2·55	3·3	0·091	2·54	2·77	3·57	1·22
Pb	19·39	14·91	27·3	18·9	1·70	2·5	4·67	2·89	3·83	7·37	2·91	2·99	2·2	5·01	2·06	7·72
Th	b.d.l.	b.d.l.	b.d.l.	b.d.l.	0·04	0·058	0·538	0·252	0·04	0·482	0·0064	0·0089	b.d.l.	b.d.l.	b.d.l.	0·0049
U	b.d.l.	b.d.l.	b.d.l.	b.d.l.	0·06	0·0231	0·398	0·038	0·054	0·143	0·0076	0·129	b.d.l.	b.d.l.	b.d.l.	b.d.l.

b.d.l., below detection limit. Full dataset is given in Supplementary Data Electronic Appendix Table 2.

Table 4: Whole-rock major and trace element data by XRF and ICP-MS

Sample:	K5B	K22	K20B	K23B	K20C	K23C	K73A	K74A	K79A	K84
Unit:	Hbl-D.	Hbl-D.	Hbl-D.	Hbl-D.	HL	HL	HL	HL	HL	HL
wt %										
SiO_2	60·50	63·87	64·34	69·80	69·33	74·97	69·23	69·54	70·06	67·9
TiO_2	0·78	0·69	0·79	0·33	0·38	0·18	0·45	0·24	0·54	0·48
Al_2O_3	13·35	13·29	16·32	14·94	15·35	13·78	15·77	14·66	15·15	15·92
FeO	7·49	6·54	5·14	3·01	3·11	1·97	3·05	2·72	3·04	3·22
MnO	0·21	0·15	0·07	0·04	0·05	0·03	0·034	0·04	0·03	0·033
MgO	3·83	2·64	1·67	1·16	0·91	0·70	0·89	0·7	0·93	0·89
CaO	5·51	4·41	3·62	2·62	3·60	2·74	3·02	1·38	1·79	2·48
Na_2O	3·61	3·73	4·26	3·87	4·52	4·17	4·47	1·85	3·42	3·75
K_2O	1·53	1·61	2·06	2·87	1·35	1·08	1·69	8	3·95	4·04
P_2O_5	0·07	0·08	0·44	0·16	0·27	0·12	0·24	0·2	0·18	0·31
LOI	0·75	0·68	0·96	0·87	0·94	0·84	0·69	0·84	0·9	1·02
Total	98·5	98·4	100·3	100·0	100·2	100·8	99·2	100·5	100·3	100·4
ppm										
Ni*	63	46	11	b.d.l.	b.d.l.	b.d.l.	b.d.l.	b.d.l.	b.d.l.	b.d.l.
V*	95	79	11	26	26	17	b.d.l.	b.d.l.	13	b.d.l.
Cr*	219	193	32	32	b.d.l.	63	b.d.l.	b.d.l.	32	b.d.l.
Sc*	53	47	b.d.l.	b.d.l.	b.d.l.	b.d.l.	b.d.l.	b.d.l.	b.d.l.	b.d.l.
Co*	23	13	n.a.	n.a.	n.a.	n.a.	n.a.	n.a.	n.a.	n.a.
Rb*	55·6	67·3	94·2	74·5	42·9	26·4	67·7	143	112	115
Sr*	178·9	169·9	217	150	236	135	234	240	225	206
Y	107·3	76·8	35·5	17·6	30·0	16·4	12·2	32·3	13·8	15·9
Zr	82·7	185·7	174	84·3	189	63·5	221	230	696	55·1
Nb	41·4	43·8	23·7	11·0	19·7	16·8	11·2	7·89	13·6	14·9
Cs	1·5	1·9	2·12	1·32	0·90	0·60	1·44	0·92	1·79	3·00
Ba*	212·3	192·0	351	575	221	136	323	2592	1041	664
La	14·8	13·8	44·4	9·64	36·2	7·66	34·4	75·2	135	87·4
Ce	45·2	35·2	84·1	19·6	70·2	14·0	64·2	130	250	168
Pr	7·6	5·8	9·71	2·29	7·97	1·80	7·06	14·1	23·6	17·4
Nd	38·7	29·1	36·7	9·53	30·3	7·62	25·2	50·0	74·8	60·1
Sm	15·4	11·5	8·21	2·70	6·85	2·30	4·60	9·95	10·2	9·97
Eu	1·9	1·4	1·48	0·81	1·39	0·77	1·14	1·54	1·22	1·24
Gd	18·7	13·7	8·15	3·31	7·04	2·83	3·79	9·25	6·67	6·94
Tb	3·5	2·5	1·25	0·58	1·10	0·51	0·49	1·33	0·73	0·76
Dy	19·6	14·0	6·80	3·34	6·04	2·98	2·49	7·07	3·52	3·59
Ho	3·9	2·8	1·33	0·70	1·17	0·62	0·45	1·31	0·58	0·59
Er	9·5	6·7	3·24	1·75	2·82	1·59	1·01	3·04	1·31	1·31
Tm	1·3	0·9	0·42	0·23	0·36	0·21	0·13	0·38	0·18	0·17
Yb	7·2	5·1	2·28	1·32	1·98	1·20	0·69	2·05	1·07	0·97
Lu	1·0	0·7	0·31	0·18	0·28	0·16	0·11	0·28	0·18	0·14
Hf	2·5	4·8	4·04	2·43	4·87	1·82	5·36	5·71	15·3	1·54
Pb	12·1	12·0	13·8	18·0	14·4	11·9	13·5	33·7	21·8	24·7
Th	2·3	1·7	10·3	1·87	9·41	0·77	9·54	20·8	24·0	38·5
U	2·0	1·2	1·66	0·99	1·43	1·28	1·22	1·81	1·36	3·46

(continued)

in both Stages 4 and 5 tends to have slightly higher Fe contents ($X_{Mg} \sim 0{\cdot}44$–$0{\cdot}46$) than biotite present in Stage 1. Locally the biotite forms aggregates several millimetres across with the accessory phases located between the grains.

Stage 6: dispersion

In the final developmental stage, schlieren have essentially disappeared and the diatexite generally becomes grey because of a higher content of dispersed ferromagnesian minerals (mostly biotite), which are oriented parallel to the magmatic flow fabric indicated by the few remaining, or nearby, schlieren. The few scattered schollen remaining are small (<2 cm) and rounded or lenticular in shape (Fig. 3d–f). This sequence suggests that flow of the diatexite is able to erode schollen and disperse the detached crystals, producing a mesocratic and homogeneous enclosing diatexite.

In summary, the sequence of features from Stages 1 to 6 is interpreted to form by the disaggregation and erosion of schollen following infiltration of melt from the enclosing diatexite and magmatic flow of the diatexite around the schollen. As a result, the host leucocratic diatexite becomes contaminated with entrained mafic material and develops a mesocratic composition (Fig. 3c).

Interaction between leucosomes and paleosome

Evidence for the entrainment of mafic minerals is also observed in some leucosomes. These contaminated leucosomes have higher modal ferromagnesian minerals than the ordinary leucosomes described by Carvalho *et al.* (2016). For instance, Fig. 6a shows a

Table 4: Continued

Sample: Unit:	K90 HL	K11 Mel.	K23A Mel.	K20A Mel.	K108D Mel.	K75 Mel.	K24 A.	Ki-04 Hbl-Gran.	Ki-34 Hbl-Gran.	17 A Hbl-Gran.
wt %										
SiO_2	70·70	57·21	57·40	60·02	60·69	61·26	48·78	68·19	62·62	69·35
TiO_2	0·44	0·90	0·85	1·13	0·76	1·42	1·01	0·262	0·09	0·123
Al_2O_3	14·32	13·06	12·61	16·77	17·64	13·69	13·53	14·63	15·91	14·94
FeO	2·38	6·40	7·72	7·10	4·32	7·21	8·80	4·36	3·44	1·66
MnO	0·03	0·12	0·15	0·10	0·09	0·10	0·24	0·03	0·074	0·043
MgO	0·80	5·72	6·17	2·37	1·57	2·70	6·05	0·01	0·94	0·51
CaO	3·04	6·93	7·06	4·27	5·06	3·26	14·40	2·05	4·94	2·34
Na_2O	4·41	3·31	2·82	4·09	5·48	3·07	2·79	3·77	3·59	3·5
K_2O	1·52	2·59	2·43	2·36	1·43	3·09	0·55	4·5	4·36	5·32
P_2O_5	0·17	0·38	0·43	0·64	0·18	0·28	0·14	0·102	0·14	0·065
LOI	0·80	1·02	1·29	0·76	0·54	0·92	0·73	0·22	1·8	0·68
Total	98·9	98·3	99·9	100·4	98·2	97·8	98·0	98·61	98·29	98·72
ppm										
Ni*	8	93	100	47	b.d.l.	34	99	b.d.l.	6	5
V*	29	b.d.l.	215	52	80	132	234	72	16	b.d.l.
Cr*	b.d.l.	262	126	b.d.l.	b.d.l.	72	268	b.d.l.	b.d.l.	b.d.l.
Sc*	8	27	b.d.l.	b.d.l.	b.d.l.	21	36	b.d.l.	16	15
Co*	n.a.	36	n.a.	n.a.	15	23	39	b.d.l.	7	b.d.l.
Rb*	59·1	142	109	122	67·6	142	3·90	79	81	106
Sr*	185	137	95·8	201	360	146	103	222	330	228
Y	14·5	40·8	37·6	50·1	19·2	77·9	26·1	9	32	31
Zr	446	167	102	394	195	1290	84·2	120	122	137
Nb	12·0	27·1	18·1	33·9	15·5	34·1	6·57	b.d.l.	b.d.l.	b.d.l.
Cs	1·51	3·55	2·76	2·80	2·47	3·13	0·05	1·06	1·32	2·56
Ba*	227	240	193	423	248	820	47·0	1229	1265	1436
La	118	19·0	16·3	49·9	14·7	498	7·46	45·2	67·5	24·9
Ce	231	43·9	39·5	95·8	28·9	814	14·9	78·3	119	51·5
Pr	22·6	6·28	6·08	11·4	3·54	76·9	2·11	7·89	12·4	6·17
Nd	75·7	29·1	29·1	44·2	14·1	242	9·66	26·5	44·6	24·8
Sm	11·4	8·77	9·08	10·2	3·21	33·1	2·87	4·43	9·32	6·78
Eu	1·19	1·13	1·05	1·85	1·03	1·81	1·08	1·15	1·53	1·26
Gd	7·51	8·96	9·75	10·5	3·18	24·1	3·46	3·46	8·77	7·20
Tb	0·81	1·43	1·49	1·66	0·54	3·03	0·63	0·38	1·27	1·11
Dy	3·71	7·50	7·89	9·19	3·09	16·5	3·92	1·68	6·58	5·95
Ho	0·57	1·42	1·50	1·85	0·62	2·98	0·88	0·26	1·19	1·15
Er	1·30	3·55	3·69	4·66	1·66	7·27	2·46	0·60	2·84	2·75
Tm	0·16	0·49	0·50	0·63	0·25	0·99	0·38	0·07	0·36	0·36
Yb	0·93	2·97	2·96	3·67	1·69	5·66	2·50	0·43	2·01	2·07
Lu	0·15	0·44	0·43	0·52	0·26	0·83	0·37	0·07	0·29	0·29
Hf	10·4	3·79	2·88	8·34	4·49	26·4	2·05	3·03	2·91	3·36
Pb	15·0	13·2	12·7	14·4	16·7	17·2	8·57	28·6	26·9	29·1
Th	45·9	5·17	3·32	13·2	4·80	66·5	1·38	16·8	18·5	9·94
U	2·01	4·18	2·41	2·89	5·27	1·37	0·81	1·68	7·10	2·80

*Trace elements.

b.d.l., below detection limit; n.a., not analysed; Hbl-D., Hbl-diatexite; HL, Hbl-leucosome; Mel., melanosome; A., amphibolite; Hbl-Gran., Hbl-granite.

leucosome of syenogranite bulk composition that traverses a scholle of mesocratic tonalite and illustrates a progressive increase in modal hornblende towards its edge. A yellow arrow (Fig. 6a) indicates where hornblende appears to be detached from the scholle and becomes incorporated into the leucosome; the passage of melt has eroded the wall of the scholle. The pinkish leucosome (Fig. 6a) has a framework of euhedral to subhedral microcline (~60%), with interstitial plagioclase (16%) and quartz (22%). Most of the hornblende in this rock is replaced by skeletal biotite, plagioclase and quartz (Fig. 5c). This suggests that the hornblende was not in equilibrium with the melt and has reacted with it to form a Bt + Pl + Qz symplectite.

Leucosomes with tonalitic bulk composition are also present in the Kinawa migmatite and have the highest hornblende and biotite contents. These leucosomes are generally associated with schollen of amphibolite, but also occur within those of metatexite (Fig. 6b). These leucosomes have a framework of euhedral to subhedral plagioclase (40–45%, $An_{23–29}$) with interstitial quartz (20–25%) and K-feldspar (10–15%; Or_{96}) and up to 14% Fe-pargasite (X_{Mg} 0·35–0·4). There is only minor replacement of amphibole by biotite (1%). The accessory phases are titanite (0·3%), apatite (0·2%) and allanite (0·15%). These leucosomes suggest that once schollen have disaggregated in the diatexites, the amphibole crystals they contribute can be carried by the diatexite magma and later segregated with the melt into younger leucosomes.

Small bodies (<2 m width) and veins of coarse-grained hornblende-bearing granodiorite occur locally

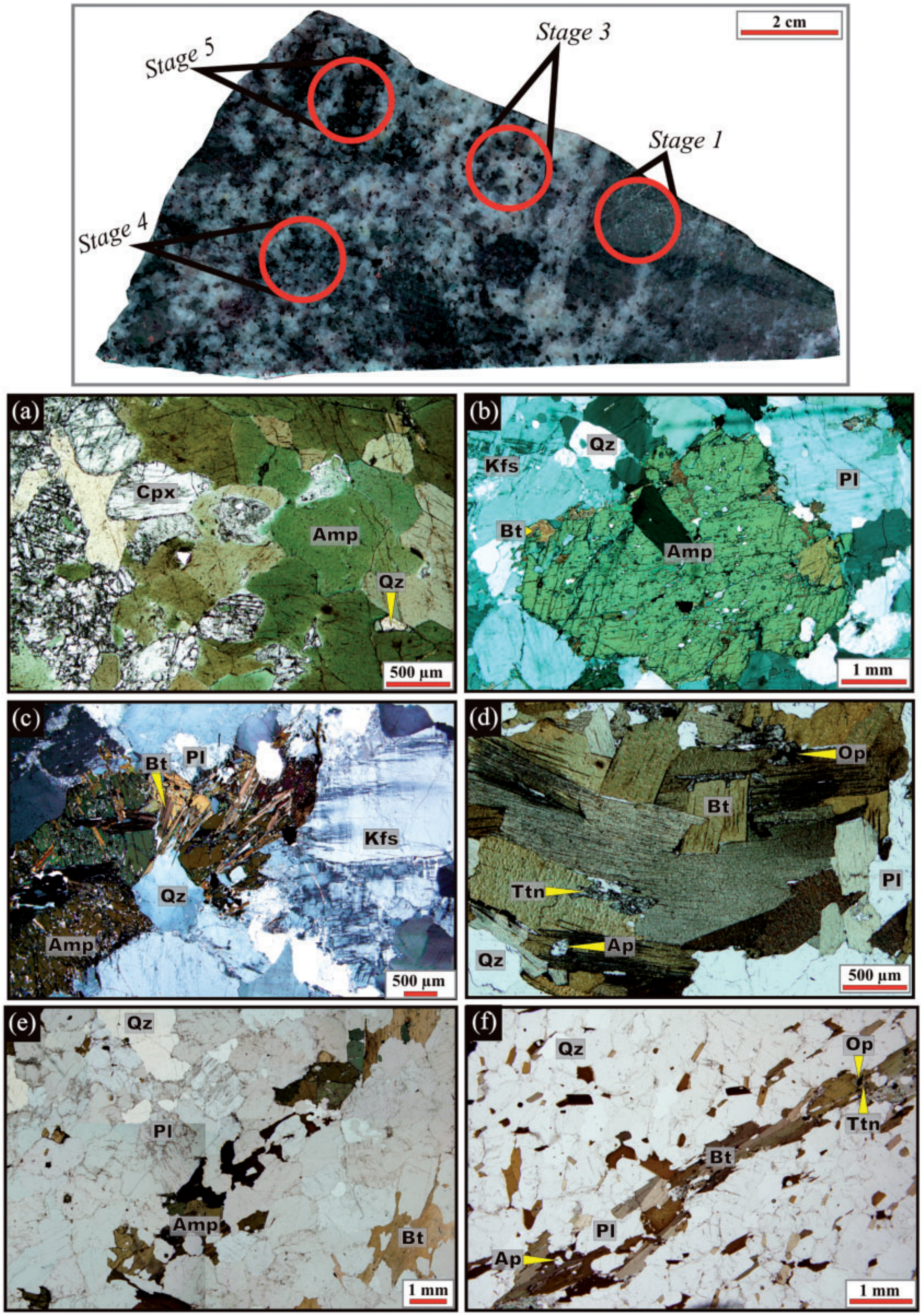

Fig. 5. Microstructural changes during the progressive disaggregation and interaction of mafic schollen with the host diatexite. Top image is of the hand sample containing four of the stages involved in the disaggregation of schollen. (a) Amphibolite fragment within diatexite (Stage 1) containing hornblende with relict light green diopside cores and interstitial quartz. This microstructure is comparable with that in the largest schollen. (b) Subhedral dark green hornblende in the host diatexite (Stage 3) consisting of subhedral plagioclase, K-feldspar and quartz. Biotite locally replaces the hornblende. (c) Hornblende partially replaced by a symplectite of biotite and quartz (Stage 4). (d) Aggregate of large, well-formed biotite crystals (Stage 5), including the accessory phases apatite and titanite. (e) Initial stage, short schlieren composed of discontinuous trains of hornblende crystals and minor biotite derived from it. (f) Later stage of long, more continuous schlieren composed of well-oriented biotite that has entirely replaced hornblende. Pl, plagioclase; Qz, quartz; Kfs, K-feldspar; Cpx, clinopyroxene; Amp, amphibole; Bt, biotite; Op, opaque minerals; Ap, apatite; Ttn, titanite.

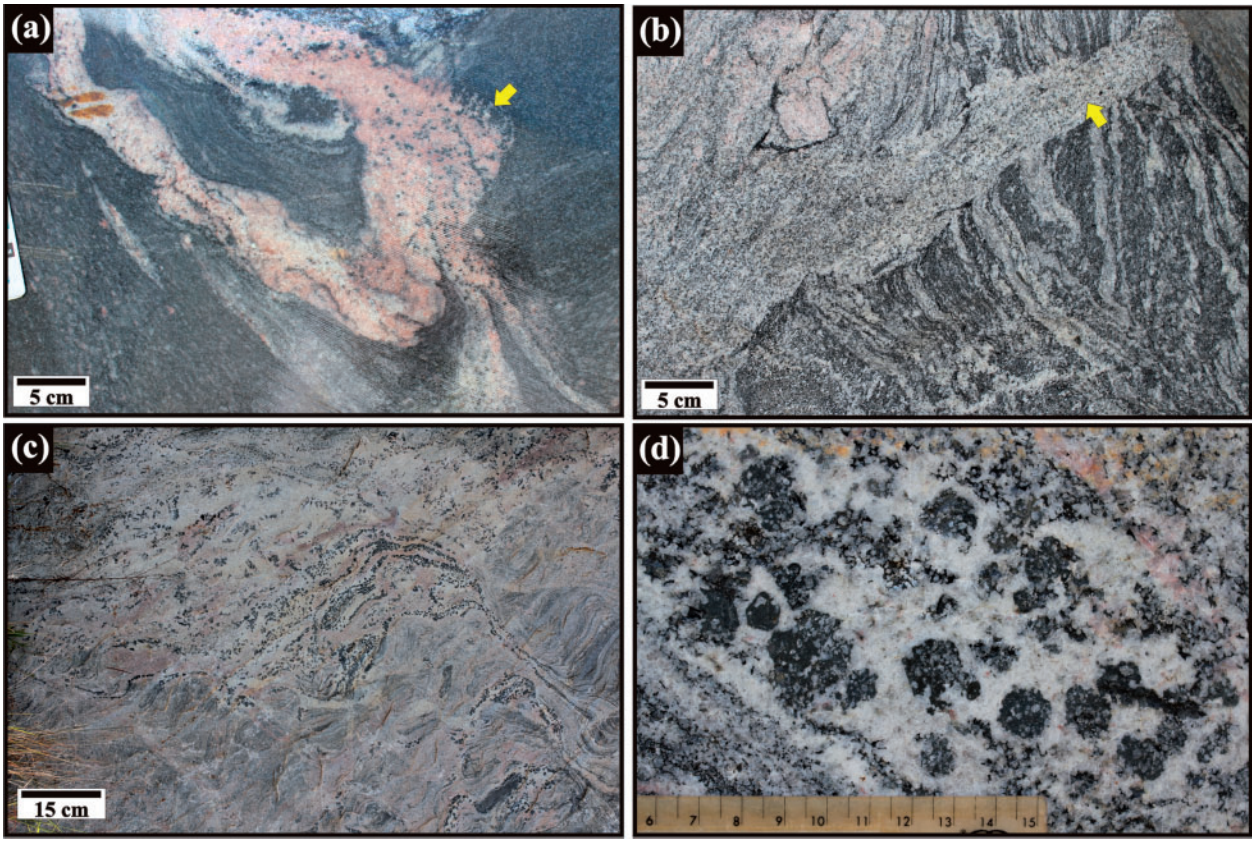

Fig. 6. (a) Pink leucosome injected into a layer of metatonalite. The yellow arrow points to the erosion of the metatonalite wall, which has contaminated the leucosome with amphibole. (b) White hornblende–biotite leucosome (see yellow arrow) crossing a scholle of metatexite. (c) Small body of the Hbl-granite (a coarse-grained hornblende-bearing granodiorite) containing large poikilitic hornblende crystals intruded into a schlieren diatexite. (d) Close-up of poikilitic hornblende containing inclusions of quartz and plagioclase; scale in centimetres.

in the Kinawa quarry, and are associated with both the schlieren diatexites and schollen of amphibolite (Fig. 6c); these are termed Hbl-granites hereafter. The hornblende crystals they contain are subhedral and poikilitic (Fig. 6d) with numerous inclusions of quartz and plagioclase; this hornblende is interpreted to have crystallized from the melt. The Hbl-granites have a heterogranular microstructure with ∼43% plagioclase ($An_{21–25}$), 33% quartz, 12% K-feldspar ($Or_{94–97}$) and up to 12% hornblende (X_{Mg} 0·46–0·49). The accessory phases are zircon (0·3%), apatite (0·5%), magnetite (0·3%) and biotite (1%).

TRACE ELEMENT CHEMISTRY OF MINERALS

The grains chosen for trace element analysis by LA-ICP-MS were selected according to their microstructural position within Stages 1, 3, 4, and 5 described above (see also summary in Table 2). Thin sections analysed were K22a and K22b (from sample K22) and K5a and K5b (from sample K5).

Plagioclase

Plagioclase crystals (Fig. 7a) from inside mafic schollen and from the surrounding diatexite were analysed and belong to Stages 1 (K22a and K5a) and 3 (K22b and K5b). All have similar (Fig. 7b) fractionated chondrite-normalized (McDonough & Sun, 1995) REE patterns with La_N/Yb_N from 50 to 150, a strong positive Eu anomaly (Eu/Eu* = 8–60) and extremely low heavy REE (HREE) contents (∼0·01 times chondrite).

Of the other trace elements that were determined, Sr and Pb have compositional ranges that differ slightly (see Supplementary Data Electronic Appendix Table 2) between Stages 1 and 3. The Pb contents do not vary much, but plagioclase from Stage 3 extends to lower values (K5b 14–20 ppm; K22b 17–20 ppm) relative to plagioclase from Stage 1 (K5a 19–20 ppm; K22a 18–23 ppm).

The Sr contents behave in a similar fashion to CaO (described in the section 'Microstructure and major element mineral compositions'; see also Table 1). The plagioclase at Stage 1 has consistently higher Sr contents (K5a 397–447 ppm; K22a 331–367 ppm) when compared with Stage 3 (K5b 324–387 ppm; K22b 309–349 ppm). There is an overlap in the composition of the plagioclase from samples K5 and K22 from Stages 1 and 3, which may indicate that some of the crystals with higher Sr are plagioclase liberated from the schollen. Once the crystals were shed, the interaction of these with the melt induced recrystallization of the material

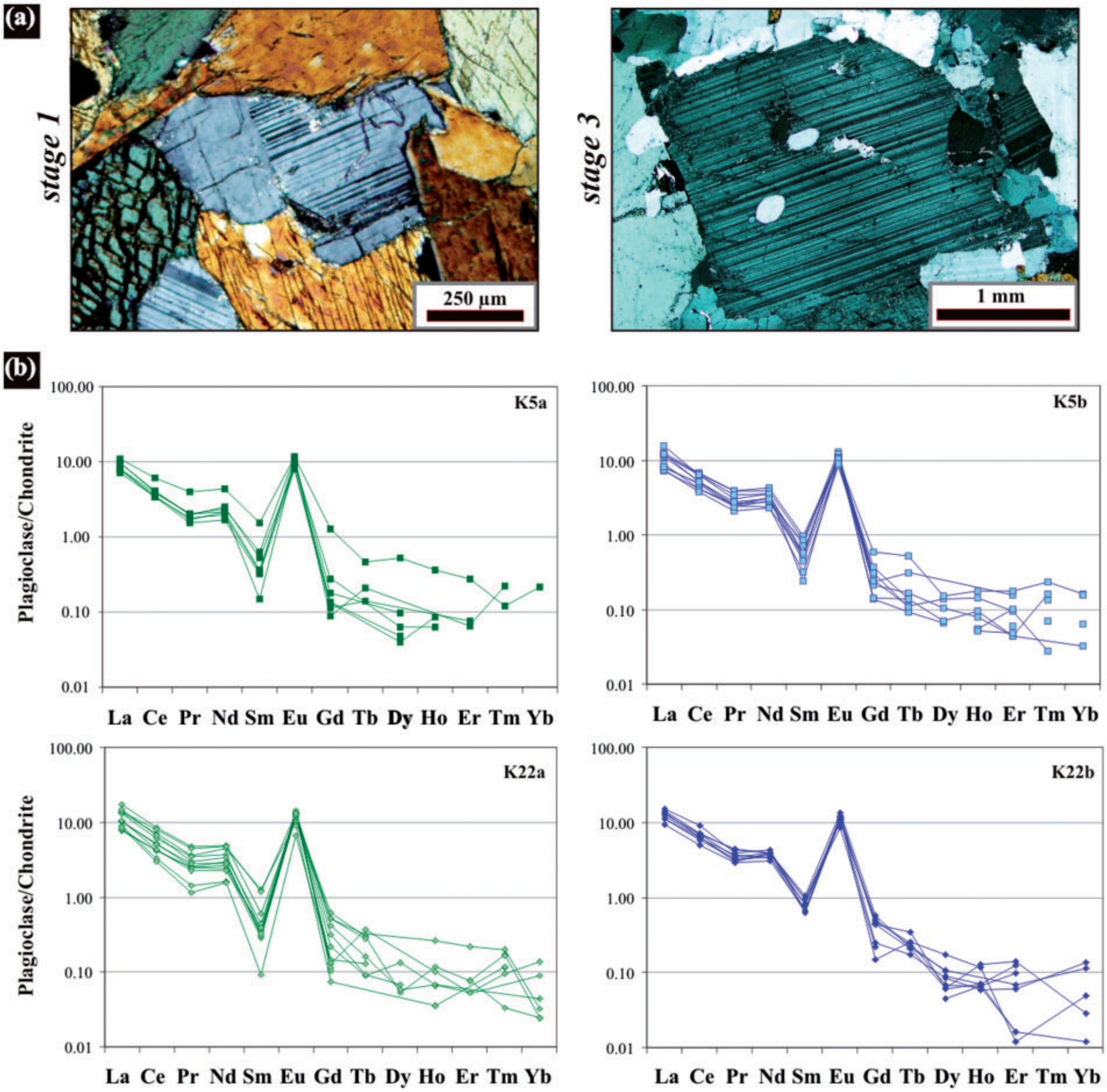

Fig. 7. (a) Left, example of plagioclase crystals in Stage 1 (K5a and K22a); right, plagioclase crystals in stage 3 (K5b and K22b). (b) Chondrite-normalized (McDonough & Sun, 1995) rare earth element patterns for plagioclase crystals from the Kinawa migmatite.

shed from the schollen and changes in the composition of the melt. Consequently, the plagioclase that crystallized from the melt after this interaction has a slightly higher Sr content than plagioclase that crystallized from the diatexite magma farther away and was not contaminated by amphibolite; this typically has ~300 ppm Sr (Carvalho *et al.*, 2016).

Clinopyroxene

Diopside (e.g. Fig. 8a) from the amphibolites contains REE at ~15 times chondrite (McDonough & Sun, 1995) in both rims and cores (Fig. 8b). REE patterns have a convex shape between La and Sm ($La_N/Sm_N \sim 0{\cdot}65$), a rather flat portion from Gd to Tm (Gd/Tm ~ 1), a distinctive negative Eu anomaly (average Eu/Eu* ~ 0·65) and slight enrichment in Yb up to 20 times chondrite. The clinopyroxene typically has high Cr (600–800 ppm), Ni (138–153 ppm), Ti (420–607 ppm) and V (153–185 ppm) contents.

Hornblende

Hornblende shows some variation in major element composition related to its microstructural position. For example, hornblende at Stage 3 has slightly higher Si and Fe contents than the crystals from Stage 1; however, the Ti contents are similar. Likewise, the trace elements display some contrasts, and also similarities, between crystals from Stages 1, 3 and 4 (Fig. 9a), which are described below.

Hornblende shows a positive correlation between Mg and Cr, Co and V (Fig. 9b). In samples K22a and K22b, Cr decreases progressively from Stage 1

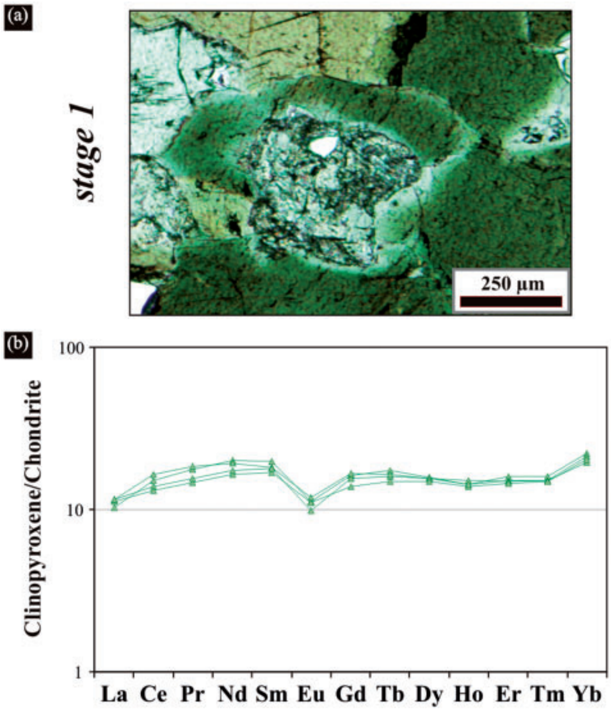

Fig. 8. (a) Example of clinopyroxene crystals in Stage 1. (b) Chondrite-normalized (McDonough & Sun, 1995) rare earth element patterns for clinopyroxene crystals of Stage 1 in the transformation of mafic schollen in the Kinawa migmatite.

(1400 ppm) to Stage 3 (342 ppm), but for samples K5a and K5b the difference is more subtle, decreasing from 535 ppm at Stage 1 to 353–458 ppm at Stages 3 and 4. Similar behaviour is shown by Co; hornblende in sample K22a has higher contents, ranging from 56–62 ppm in Stage 1 to 40–51 for Stage 3, and hornblende in K22b reaches slightly lower (38–44 ppm) Co contents in Stage 4. The Co content of hornblende from the three stages in sample K5a ranges from 48 to 51 ppm, whereas in K5b amphibole from Stage 3 has slightly lower Co contents from 40 to 46 ppm.

The Sc, ΣREE and U content of hornblende crystals show negative correlations with Mg (Fig. 9b). Stage 1 hornblende from sample K22a has the lowest contents, respectively 38–41 ppm, 160–220 ppm and 0·02–0·05 ppm, whereas hornblende grains in Stages 3 and 4 from both K22a and K22b have considerably higher contents of Sc (54–290 ppm), ΣREE (384–680 ppm) and U (0·05–1·2 ppm). In contrast, hornblende grains from Stages 1, 3 and 4 in sample K5a all have similar Sc (73–95 ppm), ΣREE (271–337 ppm) and U (up to 0·14 ppm) contents. Stage 3 hornblende in sample K5b attains much higher values, respectively 114–146 ppm, 384–524 ppm and 0·01–0·78 ppm. Figure 9c shows that the chondrite-normalized (McDonough & Sun, 1995) REE patterns for all hornblendes are similar. The main feature is a progressive enrichment from La to Sm and a strong negative Eu anomaly (Eu/Eu* $\sim$ 0·2–0·7). The REE contents for hornblende from Stages 1, 3 and 4 in sample K5a are much alike and about 100 times chondrite, with a progressive enrichment from La to Sm (La$_N$/Sm$_N$ = 0·4–0·57) and a negative europium anomaly (Eu/Eu* $\sim$ 0·3–0·45). Hornblende from sample K5b has a similar-shaped pattern, but at $\sim$150 times chondrite and with larger negative Eu anomalies (Eu/Eu* = 0·25).

Only the hornblende from samples K22a and K22b displays different shaped patterns (Fig. 9c) depending on its microstructural stage. Stage 1 hornblende has the lowest ($\sim$50 times chondrite) and flattest pattern (La$_N$/Yb$_N$ = 0·83–1·13) with a small negative Eu anomaly. In contrast, hornblende from Stage 3 (samples K22a) and Stage 4 (sample K22b) shows higher patterns with a systematic enrichment of the middle REE (MREE; Nd to Ho, except Eu) resulting in larger negative Eu anomalies (Eu/Eu* 0·16–0·3).

Biotite

Biotite grains from Stages 1 (K22a), 4 (K5a, K5b and K22b) and 5 (K5b and K22b) were analysed. All have very low REE contents that are mostly below the detection limit.

The trace elements Cr, Sc and V show negative correlations with Fe; this behaviour is similar to that observed in hornblende, which the biotite replaces. Biotite from Stage 1 (K22a) has the highest Cr content (700–1100 ppm) and lowest Fe, whereas at Stages 4 (K5a, K5b and K22b) and 5 Cr decreases to 260–560 ppm, which is still much higher than in the biotite from the homogeneous diatexites sampled far from schollen (typically $\sim$ 100 ppm; Carvalho *et al.*, 2016). The Sc content in biotite at Stage 1 is fairly uniform (21–29 ppm), but shows much greater variation (10–65 ppm) in Stages 4 and 5. Biotite from samples K22a and K22b shows similar amounts of V (215–250 ppm) at Stages 1, 4 and 5, but biotite from samples K5a and K5b has higher V contents (275–315 ppm).

WHOLE-ROCK GEOCHEMISTRY

Major elements

Whole-rock Harker diagrams in Fig. 10 include the amphibolite, melanosomes from metatexites, Hbl-diatexites, Hbl-leucosomes and Hbl-granites from the Kinawa migmatite described in this contribution. In addition, samples of Kinawa diatexites and leucosomes not contaminated by mafic rocks from Carvalho *et al.* (2016) are shown together with fields compiled for hornblende-bearing granites, hereafter called amphibole-granites (or Amp-granites), from the Superior Province (Stevenson *et al.*, 2009), the Konso pluton (Asrat & Barbey, 2003), Karakoram (Reichardt & Weinberg, 2012), leucogranites from the Opatica Subprovince (Sawyer, 1998), I-type leucogranites (Chappell, 1999), and quenched melts (glasses) from the experiments of Conrad *et al.* (1988), Johnston & Wyllie (1988) and Acosta-Vigil *et al.* (2006).

There is a good negative correlation between SiO$_2$ and the major elements CaO, FeO + MgO, TiO$_2$ and

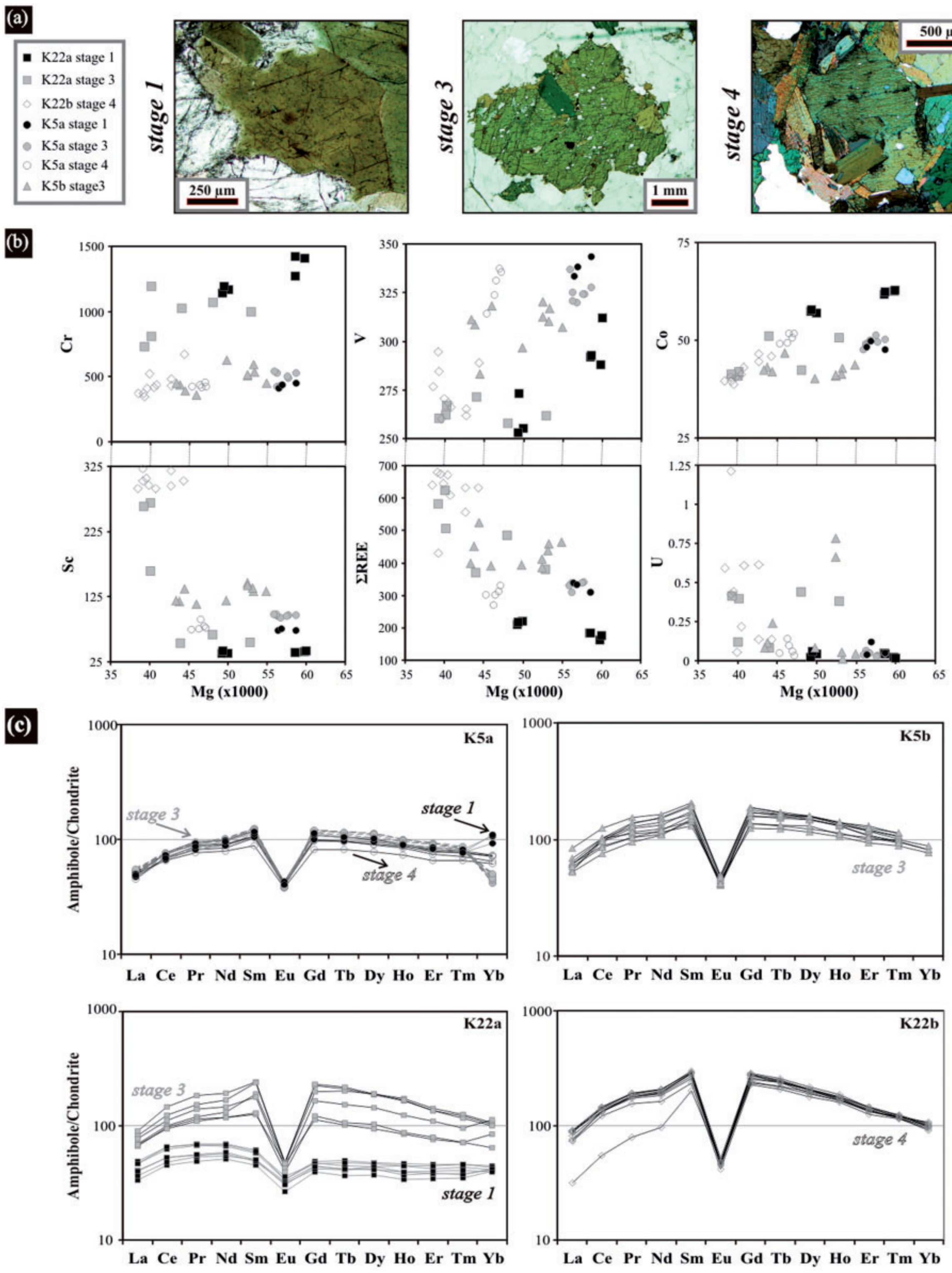

Fig. 9. (a) Photomicrographs showing three examples of the hornblende crystals analysed from Stages 1, 3 and 4, respectively, of schollen disaggregation. (b) Selected trace elements vs Mg (both in ppm). Stages 1, 3 and 4 are represented by black, grey and open symbols, respectively. (c) Chondrite-normalized (McDonough & Sun, 1995) rare earth element patterns for hornblende crystals from the Kinawa migmatite.

P_2O_5 (Fig. 10). The amphibolite has the highest FeO + MgO (15 wt %), and CaO (∼14·5 wt %; Fig. 10), high TiO_2 (∼1 wt %) and lowest SiO_2 (50 wt %) contents. One melanosome from the metatexite and three of the Hbl-diatexites have similar wide variations in FeO + MgO (6–14 wt %; Fig. 10a) and TiO_2 contents (0·75–1·4 wt %; Fig. 10b) that are considerably higher than those exhibited by Amp-granites, leucogranites

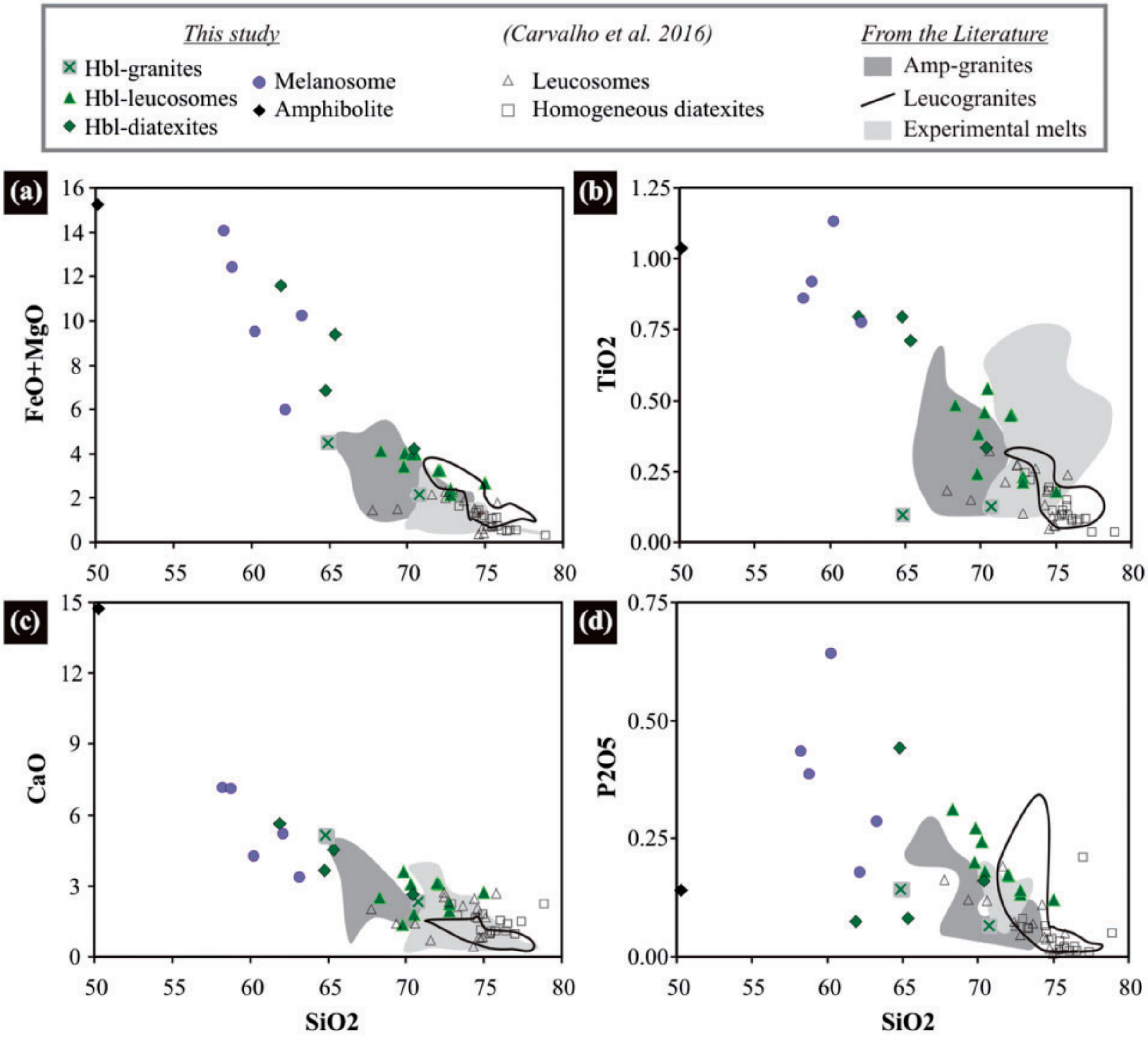

Fig. 10. Harker diagrams (in wt %) for the schollen, Hbl-diatextites, Hbl-leucosomes and Hbl-granite from the Kinawa migmatite together with the leucosomes and homogeneous diatexites from Carvalho *et al.* (2016) and data from the literature [Amp-granites from Asrat & Barbey (2003), Stevenson *et al.* (2009) and Reichardt & Weinberg (2012); leucogranites from Sawyer (1998) and Chappell (1999); experimental melts from H_2O-added partial melting of granites from Conrad *et al.* (1988), Johnston & Wyllie (1988) and Acosta-Vigil *et al.* (2006)]. (a) FeO + MgO vs SiO_2; (b) TiO_2 vs SiO_2; (c) CaO vs SiO_2; (d) P_2O_5 vs SiO_2.

and experimental melts from the literature. In contrast, Hbl-granites, Hbl-leucosomes and one Hbl-diatexite (sample K20c) have intermediate FeO + MgO and TiO_2 contents (>3 wt % and >0·25 wt % respectively), which are considerably higher than values for the homogeneous diatexites and leucosomes from Kinawa sampled far from the schollen, and the leucogranites from the studies by Chappell (1999) and Sawyer (1998), but plot mostly inside the field of Amp-granites. A similar pattern is shown by CaO; the Hbl-diatexites, Hbl-granites and Hbl-leucosomes have CaO contents (>3 wt %) that are intermediate between those of the amphibolite or melanosome and those of the Kinawa homogeneous diatexites and leucosomes (Fig. 10c).

There is a large variation in the P_2O_5 contents of melanosomes from the metatexite; sample K20A has the highest contents of all (0·6 wt %; Table 4) whereas the amphibolite has low contents. The Kinawa Hbl-leucosomes, Hbl-diatexites and Hbl-granites broadly show the same wide range as the amphibolite and melanosomes; however, most Hbl-leucosomes are more enriched in P_2O_5 at the same SiO_2 content (Fig. 10d) and form a trend that is distinctly steeper than that for the Kinawa homogeneous diatexite and leucosome sampled far from the schollen.

Trace elements

Mafic amphibolite K24 has the highest Cr (268 ppm), Ni (99 ppm) and Co (39 ppm) contents (see Table 4). The melanosome from the metatexite shows considerable variation, exhibiting both high and very low

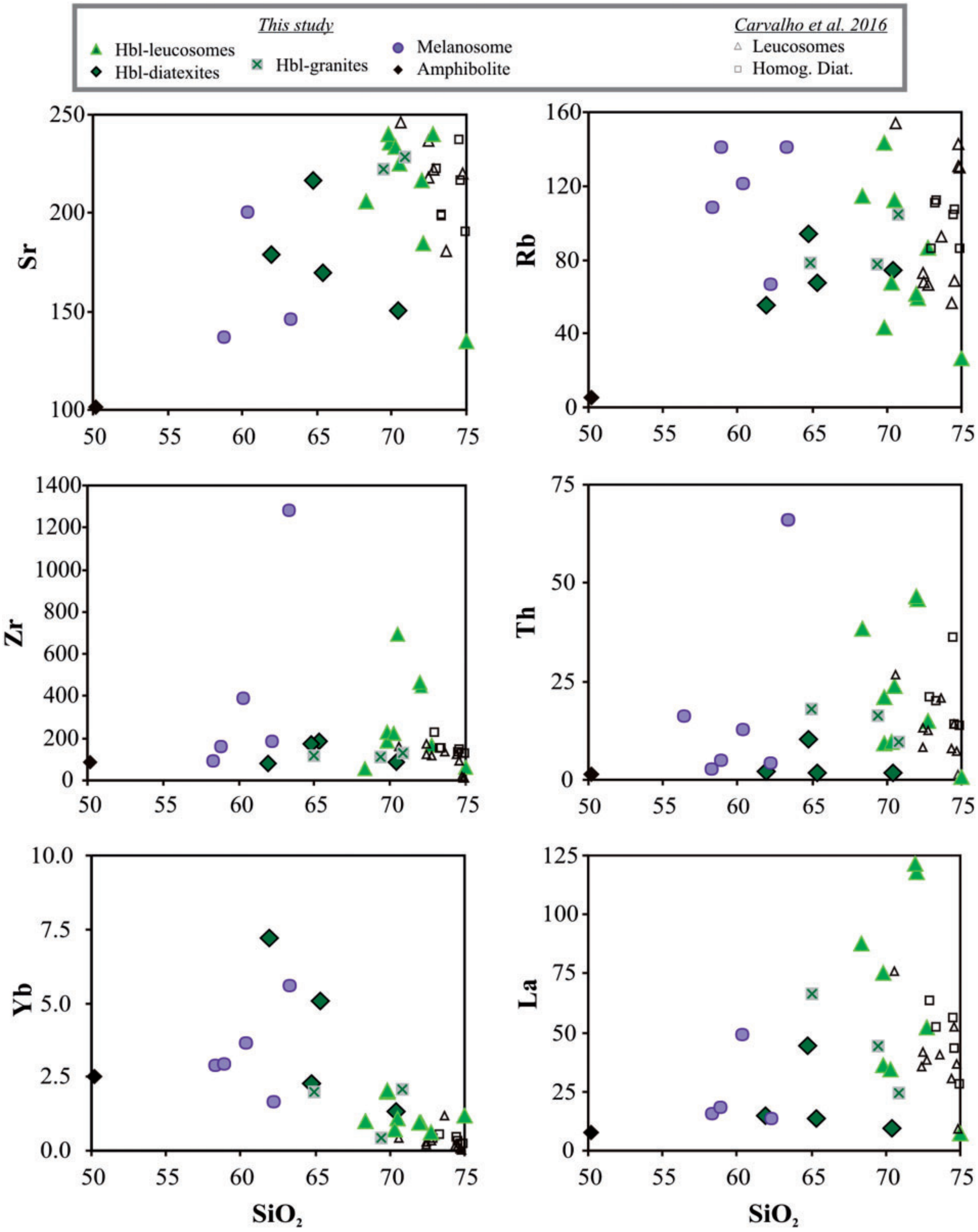

Fig. 11. Selected trace elements (ppm) vs SiO_2 (wt %) for the Kinawa migmatite including amphibolite, melanosome from metatexite schollen, Hbl-diatexites, Hbl-leucosomes and Hbl-granite from the Kinawa migmatite, together with the leucosomes and homogeneous diatexites from Carvalho *et al.* (2016).

concentrations of these elements (Table 4). The Hbl-diatexites (samples K5 and K22) also have high Cr (193–219 ppm), Ni (46–63 ppm) and Co (13–23 ppm) contents, but the Hbl-leucosomes (except K23C and K90) and the Hbl-granites have negligible amounts of these elements (mostly below detection limit) and are similar to the ordinary leucosomes and homogeneous diatexites (see Carvalho *et al.*, 2016).

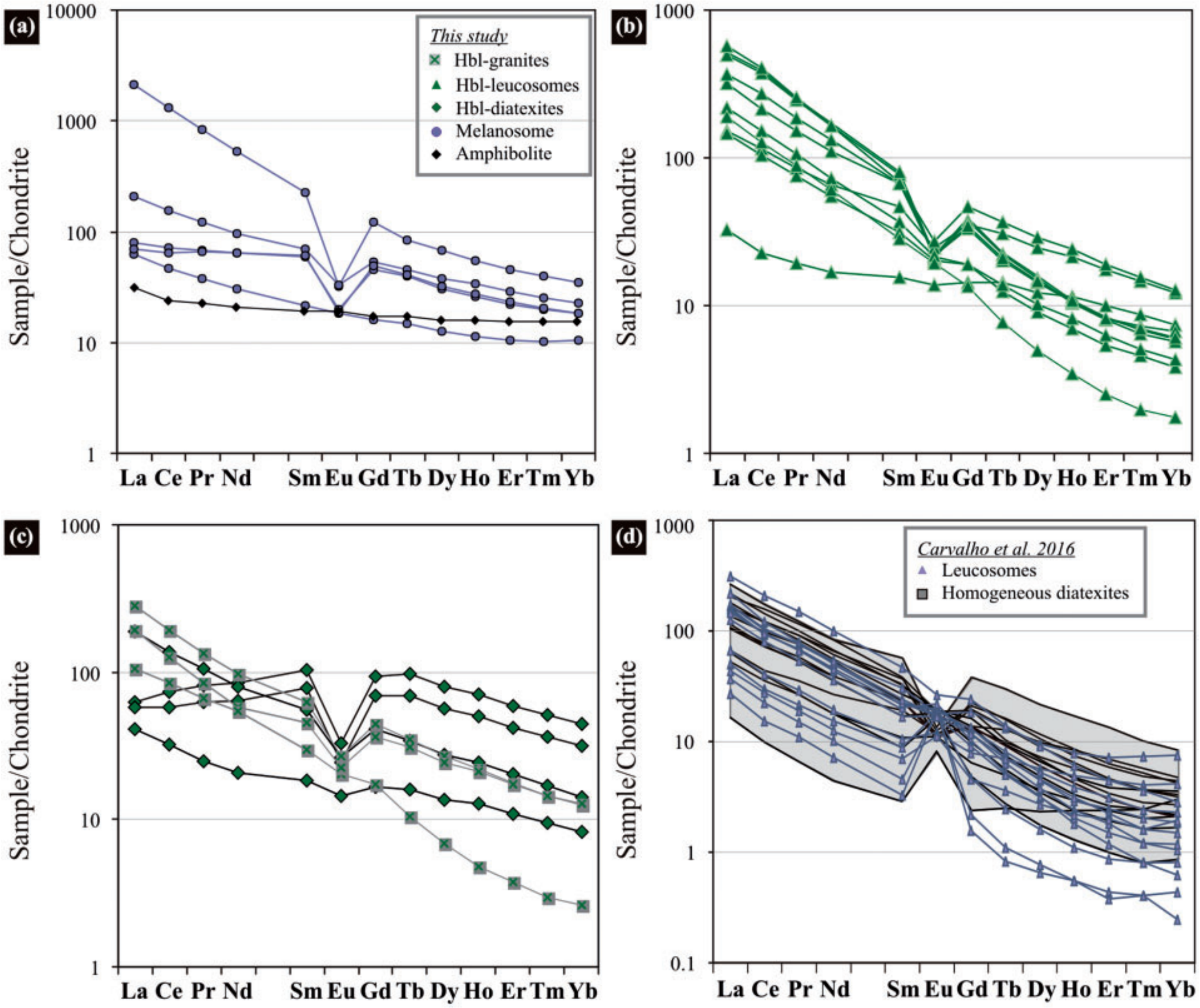

Fig. 12. (a–d) Whole-rock chondrite-normalized (McDonough & Sun, 1995) rare earth element patterns for samples of the Kinawa Migmatite. The grey shaded field in (d) represents the composition of homogeneous diatexites from Carvalho *et al.* (2016).

The other trace elements (Fig. 11) generally show a wide range in abundances between the amphibolite and melanosome, and a trend is not always apparent. The amphibolite has the lowest Sr and Rb contents and lies on a weak trend to progressively higher contents from Hbl-diatexite through Hbl-granite to Hb-leucosome. However, the pattern is a little more complex if the melanosome from the metatexites is considered as the starting point; Sr still increases, but Rb decreases from Hbl-diatexite through Hbl-granite to Hbl-leucosome.

Zirconium shows poor correlations with SiO_2. Most samples from amphibolites, melanosomes, Hbl-diatexites, Hbl-granites and Hbl-leucosomes have comparable ranges of Zr at different SiO_2. Exceptions are two melanosomes and three leucosomes that reach much higher values than most samples ($>$400 ppm Zr; see also Table 4).

Ytterbium shows a slightly negative correlation with SiO_2, and shows a trend of decreasing concentration from melanosomes through Hbl-diatexites, Hbl-leucosomes and Hbl-granites to the homogeneous diatexites and leucosomes. There is a progressive decrease from Hbl-leucosomes and Hbl-granites to the homogeneous diatexites and leucosomes. The amphibolite has even lower Yb content than most melanosome samples. In contrast, it is the Hbl-diatexites that appear to have anomalously high Yb contents, well above a leucodiatexite magma–amphibolite mixing line.

Lanthanum and Th are both lowest in the amphibolite (Fig. 11) and there is a general increase from Hbl-diatexites, Hbl-leucosomes and Hbl-granites to the homogeneous diatexites and leucosomes. However, some Hbl-leucosomes are significantly enriched in La and Th, whereas some Hbl-diatexites appear to be depleted.

Rare earth elements (REE)

Chondrite-normalized (McDonough & Sun, 1995) REE patterns are shown in Fig. 12a–d. The amphibolite has a smooth REE pattern ($La_N/Yb_N \sim 2$; Fig. 12a) at ~20 times chondrite ($\Sigma REE \sim 52$ ppm) and no Eu anomaly ($Eu/Eu^* = 1{\cdot}05$). Samples from the melanosome have steeper REE patterns with $La_N/Yb_N \sim 9$ (Fig. 12a), strong negative Eu anomalies ($Eu/Eu^* = 0{\cdot}2$–$0{\cdot}54$) and a concave-up form. There are two extremes. Sample K75 has very high contents of REE ($\Sigma REE \sim 1726$ ppm), reflecting its high modal proportion of accessory phases. In contrast, sample K108D has a lower REE content ($\Sigma REE \sim 76$ ppm), much flatter REE pattern ($La_N/Yb_N \sim 3{\cdot}2$) and no Eu anomaly ($Eu/Eu^* = 0{\cdot}98$).

The Hbl-leucosomes generally have the steepest REE patterns with $La_N/Yb_N \sim 25$–110 (Fig. 12b) and ΣREE from 169 to 509 ppm; the sample with the lowest total ΣREE has the flattest pattern. None of the Hbl-leucosomes have a positive Eu anomaly; 80% have negative anomalies ($Eu/Eu^* = 0{\cdot}39$–$0{\cdot}83$) and the others have essentially no anomaly ($Eu/Eu^* = 0{\cdot}92$–$0{\cdot}98$). These REE patterns are different from those of leucosomes and homogeneous diatexites far from mafic schollen, which have slightly lower La_N/Yb_N (~6–100; Carvalho *et al.*, 2016; Fig. 12d) and both strong positive and negative Eu anomalies ($Eu/Eu^* = 0{\cdot}3$–8), and extend to much lower total REE contents.

The Hbl-diatexites (Fig. 12c) exhibit two types of REE pattern. One, represented by samples K20C and K23C, is relatively smooth, slightly fractionated ($La_N/Yb_N \sim 5$–13; $\Sigma REE \sim 55$–208) and with a weak negative Eu anomaly ($Eu/Eu^* = 0{\cdot}55$–$0{\cdot}83$). The other, represented by samples K5 and K22, has lower La_N/Yb_N (~1·5), higher ΣREE (~142–187 ppm), an enrichment in the MREE (although the pattern could also be interpreted as like the first group, but depleted in La to Nd), and a pronounced negative Eu anomaly ($Eu/Eu^* = 0{\cdot}3$), owing to the higher MREE. The second group may differ from the first simply as a result of a much higher proportion of entrained hornblende and apatite.

The Hbl-granites (Fig. 12c) have REE patterns similar to but steeper ($La_N/Yb_N \sim 8$–22 and $Eu/Eu^* = 0{\cdot}52$–$0{\cdot}9$) than those of the first group of Hbl-diatexites. However, one of the Hbl-granite patterns shows increasing depletion in the HREE, resulting in a steeper pattern with a concave-upwards shape in this portion of the pattern.

DISCUSSION AND INTERPRETATION

Schollen–diatexite interaction at Kinawa

Macroscopic behaviour of the mafic layers

The macroscopic appearance of the diatexite and schollen indicates different deformation regimes. The diatexite was melt-bearing and therefore weak (Rosenberg & Handy, 2005) and underwent magmatic flow forming the S_2 fabric and schlieren. The presence of leucosomes in shear bands indicates that melt was expelled by the process of shear-enhanced compaction (Rutter & Mecklenburg, 2006) during flow of the diatexite magma in the Cláudio Shear Zone (Carvalho *et al.*, 2016, 2017). In contrast, the mafic layers and schollen do not contain the syn-anatectic S_2 fabric or show boudinage, thus indicating that they were stronger than the host diatexite. This interpretation is also supported by the fact that the diatexite has developed structures analogous to pressure shadows around the stiffer schollen and melt collected in these. Furthermore, the maximum principal stress (σ_1) is the same in all the layers of a heterogeneous rock undergoing deformation, but the minimum principal stress (σ_3) is lower in the strongest layers. Therefore, the differential stress ($\sigma_1 - \sigma_3$) is greatest in the amphibolite layer and that pressure difference is the driving force that moves melt (Brown *et al.*, 1995) from the surrounding diatexite into the amphibolite layer, or mafic schollen (Fig. 13a–d). In addition, if σ_3 is lower in the strong layer this may allow the magma pressure to induce tensile fracture there (Oliver *et al.*, 1990). Thus, melt (and H_2O) from the host diatexite moves to and into the mafic schollen for two reasons: (1) being stronger they develop pressure shadows, which attract melt: (2) they fracture and become dilatant, and this sucks melt in from this reservoir. Consequently, most schollen are surrounded by melt-enriched haloes (Fig. 13d) and contain melt-filled fractures of various orientations (Figs 2c and 3c, e).

The schollen contain thin mineral films of plagioclase, K-feldspar and quartz, which appear to pseudomorph former intergranular films of melt and replace a previous well-equilibrated microstructure. These melt films are critical to the disaggregation of schollen by surrounding strong hornblende crystals with a weak matrix, which facilitates grain boundary sliding and rotation of grains leading to their detachment by flow of the enclosing diatexite magma around the schollen. The melt films are wider at the rim than in the interior of schollen, suggesting either that more melting occurred towards the rim, or that melt infiltrated along the grain boundaries from the host diatexite into the amphibolites. Diopside is replaced by hornblende in the schollen, indicating rehydration of the amphibolite. The likely source of H_2O is the surrounding diatexite magma, which becomes saturated in H_2O as it crystallizes. The H_2O may then have diffused, or infiltrated, into the mafic schollen. The addition of H_2O to the amphibolite could allow melting (e.g. Stuart *et al.*, 2017) of its quartzo-feldspathic matrix at low temperatures (e.g. wet solidus ~620–690°C from 5 to 10 kbar; Palin *et al.*, 2016), resulting in weakening of the grain boundaries that could then permit infiltration of melt from the matrix (Fig. 13c). The infiltration of melt into already weakened grain boundaries in an orthogneiss has been described by Hasalová *et al.* (2008*a*, 2008*b*) as the first step in its disaggregation and the development of a diatexite.

The presence of hornblende-rich domains in some schollen may be further evidence of amphibolite–melt interactions. Daczko *et al.* (2016) interpreted the modification of gabbroic gneisses to hornblendites as evidence for the interaction of a hydrous, silicate melt with metagabbro.

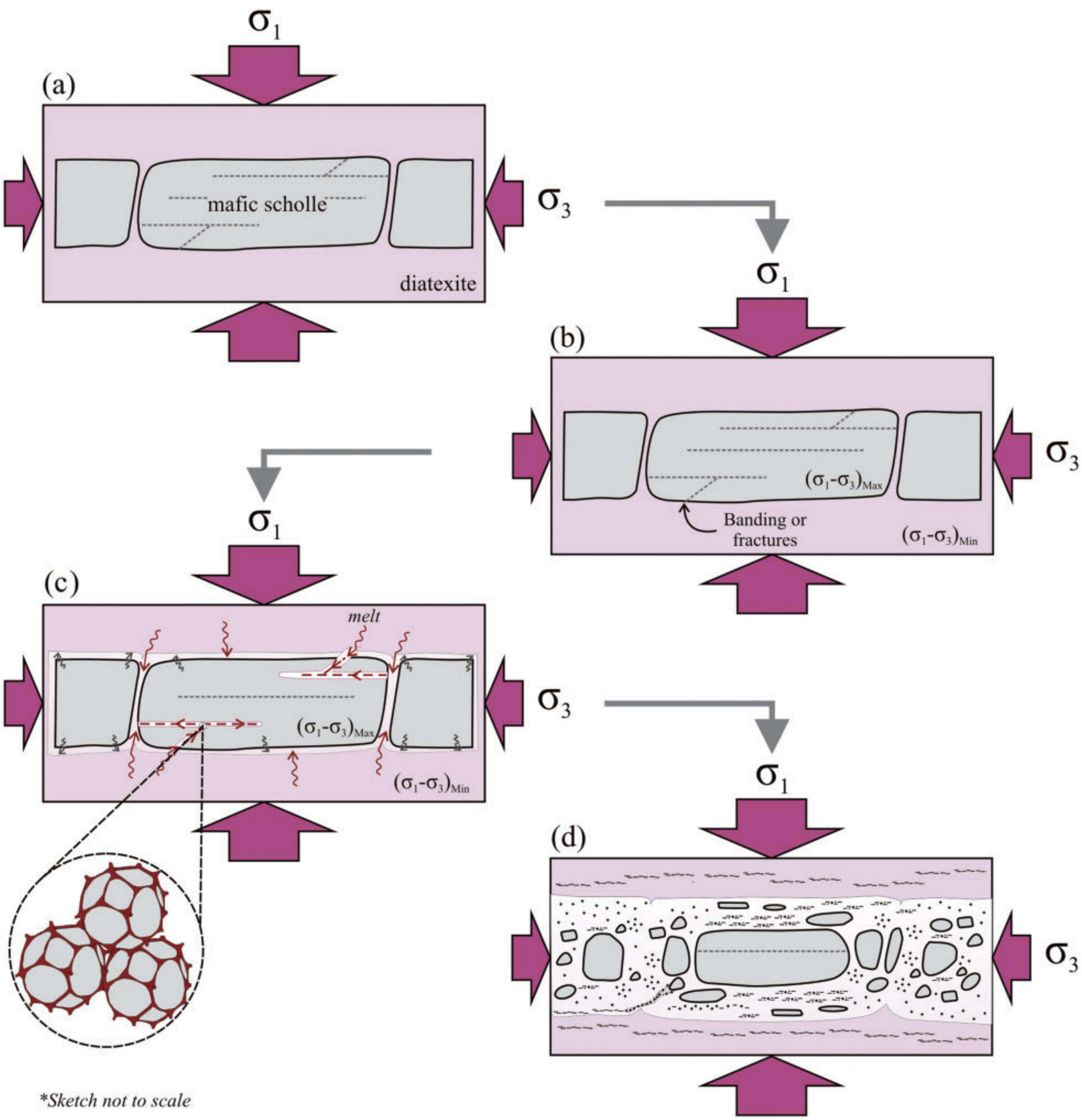

*Sketch not to scale

Fig. 13. Sketch depicting the interaction between schollen and diatexite. The process begins with (a) the migration and accumulation of melt in low-pressure sites (e.g. necks of boudins of mafic rock), progresses with (b) and (c) percolation of melt along banding and fractures, and terminates with (d) the disaggregation of the scholle into the diatexite.

Mineral composition after the interaction

Interaction with the infiltrating H_2O and melt progressively changes the composition of the minerals. For example, plagioclase becomes less calcic from the interior ($\sim An_{45}$) to the exterior ($\sim An_{25}$) of the schollen, and it is slightly more calcic ($\sim An_{28}$) in the enclosing diatexite than in the diatexite farther away ($\sim An_{25}$). These changes in composition are likely to be the result of recrystallization of the plagioclase after reacting with the melt (e.g. Acosta-Vigil *et al.*, 2006).

The rims of biotite that replace hornblende become wider towards the edge of schollen and indicate the extent to which K_2O and H_2O, and therefore melt, penetrated. Hornblende crystals detached and isolated in the diatexite show progressively more and eventually complete pseudomorphing by biotite. This may be a function of their residence time in the diatexite, or the larger volume of diatexite magma with which to react. Hornblende inside the schollen has higher Mg#, Cr and Co, whereas disaggregated hornblende in Stages 3 and 4 has lower Mg#, Cr and Co, but higher SiO_2, Sc, REE and U. One possible interpretation of the higher Sc, REE and U is that during the partial replacement of hornblende by biotite these elements are not partitioned into biotite and so become concentrated in the remaining hornblende.

The biotite that replaces hornblende also has lower Mg# and Cr contents at Stages 4 and 5. The Mg# is ~54 for the amphibolite and ~26 for the average diatexite, thus as the shed crystals re-equilibrate with the diatexite magma they change composition. In the final stage of the disaggregation process the composition of the hornblende (and the biotite that replaces it) scattered in the diatexite will be buffered by the far larger external reservoir (e.g. Lavaure & Sawyer, 2011) of ordinary diatexite magma.

Entrainment and change in bulk composition at Kinawa

Field, microstructural and geochemical relations indicate that some Kinawa diatexites and leucosomes are contaminated around schollen. The composition of the mixed rocks should define a linear trend between the diatexite magma and the schollen if complete entrainment occurred following disaggregation. Figures 10 and 11 show that this is not the case for all elements. This may arise because there are two significantly different potential sources of entrained material, the mafic schollen and the melanosomes from metatexite schollen. Alternatively, the entrainment process may have been selective to some degree, as proposed for some S-type granites (Stevens *et al.*, 2007; Villaros *et al.*, 2009), and not wholesale.

Geochemical mass-balance modelling was undertaken to examine and better constrain exactly which and how much of the lithologies represented in the schollen are contaminants in the anatectic magma at Kinawa. The modelling examined two aspects of this interaction. The first evaluated the selective entrainment of hornblende, biotite and plagioclase by mass-balance mixing between the assumed composition of the initial anatectic melt (sample K87 from Carvalho *et al.*, 2016) and the composition of minerals from Supplementary Data Electronic Appendix Table 3. The second simulated wholesale entrainment by mixing the bulk composition of the amphibolite (K24) and average melanosome with anatectic melt (K87). The term wholesale entrainment describes a process that has the equivalent compositional consequence to the well-known process of bulk assimilation. However, wholesale entrainment implies that all the solid present in the schollen is entrained in the melt but does not necessarily dissolve into it, although it might in some cases. Results of the model are shown in Fig. 14 and in Supplementary Data Electronic Appendix Table 3.

Figure 14a shows that $FeO + MgO$ and TiO_2 versus SiO_2 for some Hbl-leucosome samples falls close to the mixing line between melt and amphibolite but CaO versus SiO_2 does not. Because of the low proportion of Hbl in the melanosomes, the mixing between melanosome and melt clearly could not account for the mineral assemblages with Hbl, but it explains reasonably well the whole-rock composition of some Hbl-leucosomes, and one Hbl-granite, especially for CaO. However, in terms of $FeO + MgO$, CaO and TiO_2, the Hbl-diatexites (K5B and K22) are much closer to the model lines for entrainment of only hornblende and biotite; thus, selective entrainment may have occurred in these samples. The mixing line for plagioclase provides a good fit for samples of Hbl-granite (K17A and K34), but only in terms of TiO_2, because they exhibit much lower contents than the other Hbl-bearing samples. Some Hbl-diatexites and Hbl-leucosomes have very high TiO_2 contents and as these were probably not derived from the melanosome, because this has little or no hornblende, it is likely that these result from the selective enrichment of titanite or ilmenite and hornblende.

Contamination of diatexite by entrainment has a strong influence on the content of the REE (Fig. 14b) in the resulting rocks. Drummond *et al.* (1996) and Reichardt & Weinberg (2012) have shown that the accumulation of hornblende in the source can produce leucogranites with high La_N/Yb_N. In contrast, Hu *et al.* (2016) found that entrainment of hornblende was a key feature in lowering the La_N/Yb_N of leucosomes from the North Dabie Zone. The entrainment of hornblende into the melt at Kinawa clearly lowers the La_N/Yb_N ratios (Fig. 14b). Some Hbl-diatexites (K5 and K22) have REE patterns essentially parallel to those of the Kinawa hornblende (Fig. 9c) and the abundance of HREE indicates up to 30% Hbl entrainment. Hbl-diatexite K20B also follows the mixing model, but requires only about 10% entrainment (Fig. 14b, left); the reduced hornblende component results in a slightly steeper REE pattern and smaller Eu anomaly ($Eu/Eu^* \sim 0{\cdot}55$). Less entrainment (~5%) is indicated for Hbl-granites K17A and K34 (Fig. 14b, right), which have similar less fractionated REE patterns ($La_N/Yb_N \sim 15$) with negative Eu anomalies ($Eu/Eu^* \sim 0{\cdot}5$). These examples point to the preferential entrainment of hornblende rather than wholesale entrainment of amphibolite.

Model lines for wholesale entrainment of the amphibolite (various greys, Fig. 14b) do not fit the REE patterns in the Hbl-diatexites. However, two Hbl-leucosomes (K73A and K88) and one Hbl-granite (K4) follow the model lines fairly well and indicate up to ~15% wholesale entrainment.

From anatectic melt to granite; inferences from Kinawa

The compositional fields defined by I-type granites (Clemens *et al.*, 2011) and S-type granites (Garcia-Arias & Stevens, 2016) are shown in Fig. 14a. The typical Kinawa homogeneous diatexites and leucosomes lie at the high silica and low $FeO + MgO$, CaO and TiO_2 ends of the I-type granite field, appropriate to their very leucocratic nature owing to a leucogranodiorite protolith. The migmatites that have been contaminated by the disaggregation of amphibolite schollen, the Hbl-diatexite,

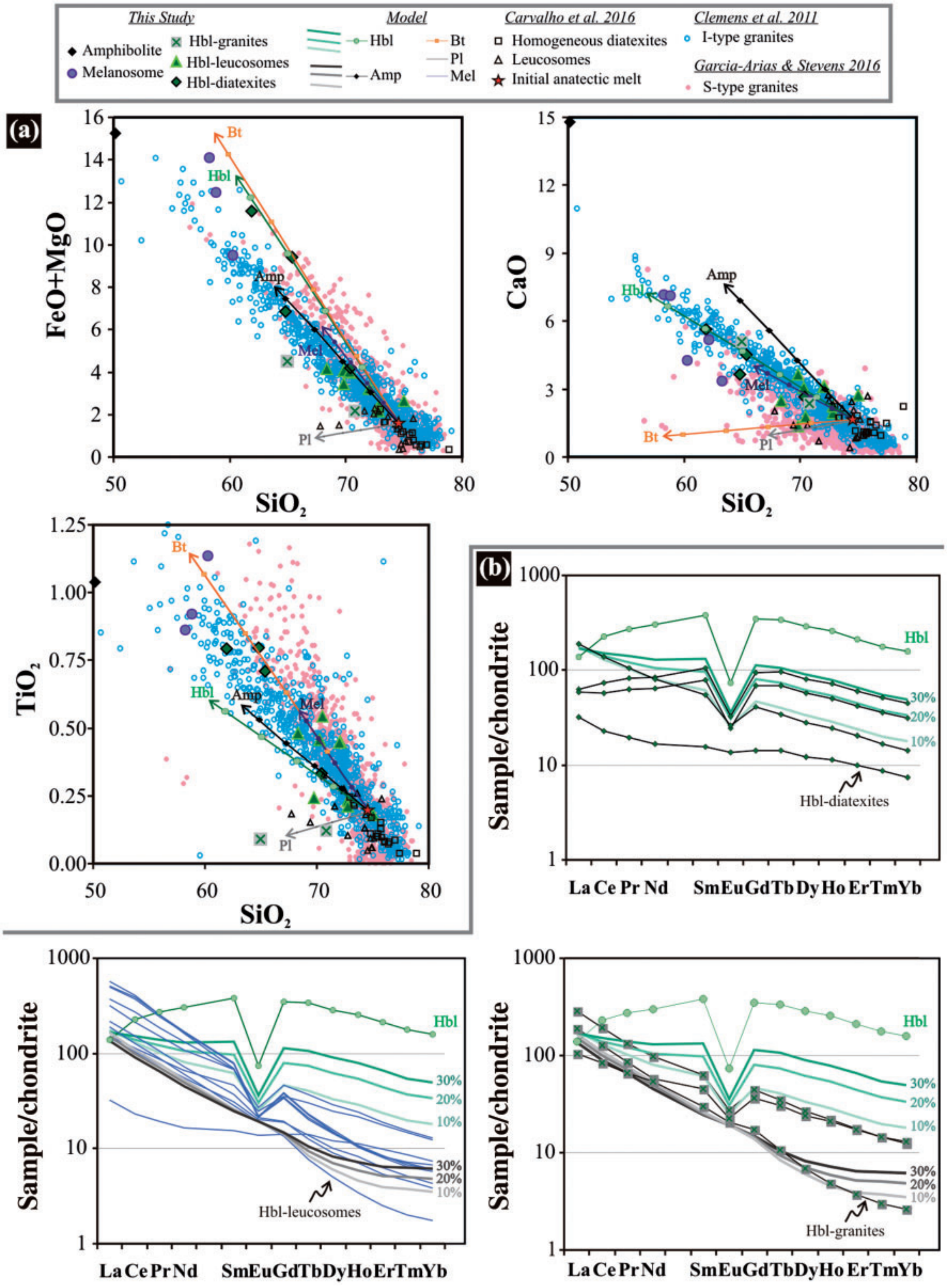

Fig. 14. Summary results of the geochemical modelling. (a) FeO + MgO vs SiO_2, CaO vs SiO_2 and TiO_2 vs SiO_2, representing the principal constituents implicated in the ‘maficity’ of granitic magmas. The mixing lines are marked at 10% increments and are for mixing between amphibolite (Amp), melanosome from metatexite (Mel), hornblende (Hbl), biotite (Bt), plagioclase (Pl) and anatectic melt [sample K87 from Carvalho *et al.* (2016)]. (b) Chondrite-normalized (McDonough & Sun, 1995) rare earth element patterns for hornblende and samples of Hbl-diatexite, Hbl-leucosome and Hbl-granite compared with model lines for the entrainment of hornblende (shades of green) and for the wholesale entrainment of amphibolite (shades of grey) into the anatectic melt.

Hbl-leucosomes and Hbl-granites, form a trend (Fig. 14a) along the centre of the I-type granite field to 7 wt % FeO + MgO and 5·7 wt % CaO, which places them beyond the bulk of I-type granites, and therefore with those of higher maficity. Two samples attain 12 wt % FeO + MgO, and lie just above the I-type field and at slightly higher SiO_2 contents; these match the highest maficity granites in both the I-type and S-type granite fields. Comparing the mixing lines for Kinawa anatectic melt and hornblende, the field for I-type granites lies at lower FeO + MgO and matches CaO, consistent with wholesale entrainment of amphibolite, or a combination of hornblende and plagioclase into the anatectic melt to make a granite magma. On the other hand, S-type granites have consistently lower CaO, but higher TiO_2 than the model trends, which indicates that, as expected, entrainment of hornblende or amphibolite alone is less important. The I-type granite field lies at higher TiO_2 than either hornblende or the amphibolite, which implies selective addition of a TiO_2-bearing phase, ilmenite or titanite, both common accessory phases at Kinawa, or that the amphibolites at Kinawa have anomalously low TiO_2 contents compared with most mafic rocks in the deep continental crust.

The composition of granite plutons differs from that of experimental melts (Conrad *et al.*, 1988; Acosta-Vigil *et al.*, 2006), leucosomes in migmatites (Sawyer, 1996) and melt inclusions in peritectic phases (Acosta-Vigil *et al.*, 2007; Cesare *et al.*, 2015) in that the majority of granites are more mafic. Other differences pertain to the relative proportions of plagioclase, quartz and K-feldspar within granite suites. These differences have been ascribed to several mechanisms (Fig. 15): (1) crystal fractionation (Tindle & Pearce, 1981; Sawyer, 1987; Chappell & White, 1992; Erdmann *et al.*, 2009); (2) magma mixing (Chappell, 1996; Kemp *et al.*, 2007; Reichardt *et al.*, 2010); (3) restite unmixing (White & Chappell, 1977; Chappell *et al.*, 1987); (4) the entrainment, selective or not, of peritectic phases (Stevens *et al.*, 2007; Villaros *et al.*, 2009; Taylor & Stevens, 2010; Clemens *et al.*, 2011; Garcia-Arias & Stevens, 2016); (5) assimilation of xenoliths and wall-rocks (Clarke & Carruzzo, 2007). All of these processes, except the first, involve contamination of anatectic melt with a ferromagnesian component to augment maficity. Recently, attention has focused on the source region where melting occurs, on assessing the relative importance of restite unmixing and the related, but more restricted, process of the entrainment of peritectic phases to explain the high FeO + MgO contents, or maficity (e.g. Clemens *et al.*, 2011), of most granites. Little attention has been paid to the physical processes by which contamination, or entrainment, might occur.

The identification of the mechanisms that operated in the source region is difficult once the melts have ascended to form a granite pluton. Migmatites, however, provide a window to the region where anatectic melts become granitic magmas and are the best place to investigate the physical process of how contamination might increase maficity. In a microstructural study, Sawyer (2014) showed that material in the source region of metatexite migmatites is entrained wholesale at the very earliest stage of melt segregation, when melt collects into the first leucosomes. The mechanism that allows entrainment is rupture of the bridges of country rock, as lenticular microleucosomes link to form macroscopic leucosomes.

The Kinawa diatexite migmatite reveals another mechanism that results in an increase in maficity: the disaggregation and entrainment of the less fertile, paleosome lithologies, such as amphibolite, that are also present in the source region. At Kinawa, the disaggregating paleosome is mafic, and the protolith to the migmatite is leucogranodiorite; thus contamination with mafic paleosome has a much greater effect than contamination with the residuum, which because of the leucocratic protolith is mainly composed of plagioclase and quartz (see Carvalho *et al.*, 2016). In some rocks the entrainment appears to be wholesale, but in others a particular phase, such as hornblende, is preferentially entrained. The changes in composition are most obvious for the major oxides, FeO + MgO, TiO_2, CaO and SiO_2, but also include trace elements such as the REE. As a consequence, melts that were felsic become magmas that are more mafic and the contaminated samples acquire compositions comparable with those of mesocratic and melanocratic I-type granites and with those of amphibole granites found around the world.

Another effect of the wholesale entrainment process at Kinawa concerns the origin of the heterogeneous isotopic signature of magmatic zircons in I-type and S-type granites noted by Belosouva *et al.* (2006) and others. Recent literature has shown that the Hf isotope signatures of magmatic zircon may vary widely, even at the thin-section scale [e.g. up to 8 εHf units in an S-type granite studied by Farina *et al.* (2014)], implying that micro-environments of different chemistry and isotope signature existed at the magmatic stage, during the growth of this mineral. Farina *et al.* (2014) interpreted this feature as a result of dissolution of inherited zircons of different Hf isotopic composition in a magma that had insufficient time to homogenize efficiently as magmatic zircon crystallized quickly. We suggest that such isotope variation might also be generated when new zircon crystallizes at the interfaces between a granitic melt and any solid material being incorporated, such as during wholesale entrainment. As an example, our amphibolite sample K24 (~80 ppm Zr, 2 ppm Hf) has Lu/Hf = 0·18 (Table 4), which is much higher than the median value of either the homogeneous diatexites or leucosomes [~0·02; data from Carvalho *et al.* (2016)]. Zircon is nearly absent, and Zr might reside largely in the original hornblende (37–56 ppm Zr in crystals from hornblende diatexite; see Table 3) and probably titanite (not analysed) also, but is almost absent in the biotite that replaces hornblende. The whole-rock Hf isotope ratio (not analysed)

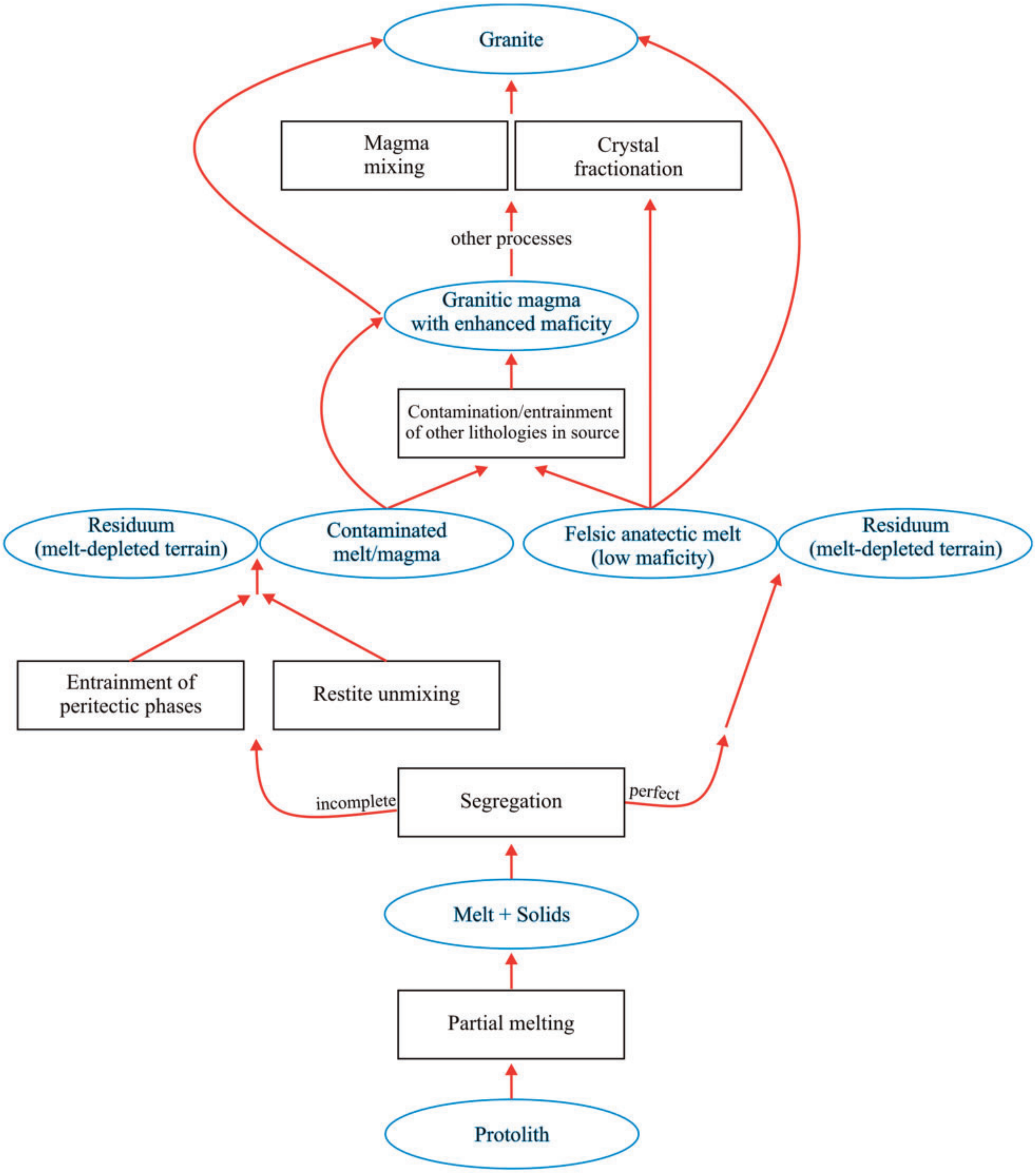

Fig. 15. Chart summarizing the sequence of processes, and the broad rock types they produce, involved in generating a granitic magma of moderate to high maficity from a felsic anatectic melt. The processes are shown in black rectangles, whereas the rock types produced are shown in blue ellipses.

should be distinct (less negative) at the time of anatexis, relative to the partial melts reacting with it (see Carvalho *et al.*, 2017). Any new magmatic crystals forming at the amphibolite–melt interface may be influenced by this contrast, and possibly would retain it, as solid–melt diffusion should be slow relative to melt–melt diffusion.

CONCLUSIONS

Disaggregation of non-protolith lithologies plays an important role in the formation of typical granitic magmas in migmatites by providing a source of the components necessary to increase the ‘maficity’ of anatectic melts generated from the fertile lithologies. Six stages of change were identified in the diatexite migmatites at

Kinawa: Stage 1, coherent mafic schollen in the diatexite; Stage 2, infiltration of melt along discontinuities and the start of chemical modification of the schollen; Stage 3, disaggregation of schollen and formation of swarms of detached hornblende crystals in the diatexite; Stage 4, partial replacement of hornblende by biotite; Stage 5, replacement of hornblende by aggregates of biotite, flow of the diatexite and formation of biotite schlieren in the host diatexite; Stage 6, flow of the diatexite, loss of schlieren and homogeneous distribution of biotite.

The interaction between melts and solid material (both paleosome and residuum) in the source is complex and differs from sample to sample. In some entrainment is essentially wholesale, whereas for others it favours certain minerals, most commonly hornblende at Kinawa, but in some cases plagioclase and a TiO_2-bearing phase. Entrainment of material as the mafic schollen disaggregate is responsible for adding $FeO + MgO$, TiO_2, CaO, Cr, Sc and Co and REE to the felsic melts produced by the anatexis of a leucogranodiorite protolith. Changes to the REE are principally the result of contamination by hornblende and include a decrease in La_N/Yb_N. Interaction between the entrained material and the host diatexite progressively changes the mineral assemblage; entrained hornblende is converted to biotite and entrained plagioclase becomes more sodic.

Entrainment of material in the source in the Kinawa migmatite involves more than simple unmixing of the residuum and entrainment of the peritectic phases. It also includes the wholesale entrainment of the other lithologies, some of which may not have melted or else melted little, that were present in the region undergoing anatexis.

ACKNOWLEDGEMENTS

This article is part of the first author's PhD thesis. The authors are grateful for all the support given by Mineração FONTEX during our visits to the Kinawa Quarry. Constructive reviews by editor James Beard and Federico Farina helped to improve this contribution, and were greatly appreciated. Antonio Acosta-Vigil is also acknowledged for his thorough comments and discussion of an earlier draft of this paper. Renato Henrique-Pinto is thanked for his support and discussions on the subject.

FUNDING

This research was funded by a Natural Sciences and Engineering Research Council of Canada Discovery Grant (RGPIN/03694-2015) to E.W.S. and a FAPESP Grant (2015/01817-6) to V.A.J. B.B.C. acknowledges the Fonds de Recherche Nature et Technologies du Québec for the award of a PhD scholarship.

SUPPLEMENTARY DATA

Supplementary data for this paper are available at *Journal of Petrology* online.

REFERENCES

Acosta-Vigil, A., London, D. & Morgan, G. B., VI (2006). Experiments on the kinetics of partial melting of a leucogranite at 200 MPa H_2O and 690–800°C: Compositional variability of melts during the onset of H_2O-saturated crustal anatexis. *Contributions to Mineralogy and Petrology* **151**, 539–557.

Acosta-Vigil, A., Cesare, B., London, D. & Morgan, G. B. (2007). Microstructures and composition of melt inclusions in a crustal anatectic environment, represented by metapelitic enclaves within El Hoyazo dacites, SE Spain. *Chemical Geology* **237**, 450–465.

Alkimin, F. F. & Marshak, S. (1998). Transamazonian Orogeny in the Southern São Francisco Craton Region, Minas Gerais, Brazil: evidence for Paleoproterozoic collision and collapse in the Quadrilátero Ferrífero. *Precambrian Research* **90**, 29–58.

Asrat, A. & Barbey, P. (2003). Petrology, geochronology and Sr–Nd isotopic geochemistry of the Konso pluton, south-western Ethiopia: implications for transition from convergence to extension in the Mozambique Belt. *International Journal of Earth Sciences* **92**, 873–890.

Ávila, C. A., Teixeira, W., Bongiolo, E. M., Dussin, I. A. & Vieira, T. A. T. (2014). Rhyacian evolution of subvolcanic and metasedimentary rocks of the southern segment of the Mineiro belt, Sao Francisco Craton, Brazil. *Precambrian Research* **243**, 221–251.

Baltazar, O. F. & Zucchetti, M. (2007). Lithofacies associations and structural evolution of the Archean Rio das Velhas greenstone belt, Quadrilátero Ferrífero, Brazil: a review of the setting of gold deposits. *Ore Geology Reviews* **32**, 471–499.

Belousova, E. A., Griffin, W. L. & O'Reilly, S. Y. (2006). Zircon crystal morphology, trace element signatures and Hf isotope composition as a tool for petrogenetic modelling: examples from Eastern Australian granitoids. *Journal of Petrology* **47**, 329–353.

Brown, M., Averkin, Y. A., McLellan, E. L. & Sawyer, E. W. (1995). Melt segregation in migmatites. *Journal of Geophysical Research* **100**, 655–679.

Campos, J. C. S., Carneiro, M. A. & Basei, M. A. S. (2003). U–Pb evidence for Late Neoarchean crustal reworking in the southern Sao Francisco Craton (Minas Gerais, Brazil). *Anais da Academia Brasileira de Ciencias* **75**, 497–511.

Carneiro, M. A., Carvalho Júnior, I. M. & Teixeira, W. (1998). Ensialic tectonic setting of the Archaean Rio das Velhas greenstone belt: Nd and Pb isotopic evidence from the Bonfim Metamorphic Complex, Quadrilátero Ferrífero, Brazil. *Brazilian Journal of Geology* **28**, 189–200.

Carvalho, B. B., Sawyer, E. W. & Janasi, V. A. (2016). Crustal reworking in a shear zone: transformation of metagranite to migmatite. *Journal of Metamorphic Geology* **34**, 237–264.

Carvalho, B. B., Janasi, V. A. & Sawyer, E. W. (2017). Evidence for Paleoproterozoic water-fluxed anatexis of Archean crust along a shear zone: a case study of the Kinawa migmatite, southern São Francisco Craton, Brazil. *Precambrian Research* **291**, 98–118.

Cesare, B., Acosta-Vigil, A., Bartoli, O. & Ferrero, S. (2015). What can we learn from melt inclusions in migmatites and granulites? *Lithos* **239**, 186–216.

Chappell, B. W. (1996). Magma mixing and the production of compositional variation within granite suites: Evidence from the granites of southeastern Australia. *Journal of Petrology* **37**, 449–470.

Chappell, B. W. (1999). Aluminium saturation in I- and S-type granites and the characterization of fractionated haplogranites. *Lithos* **46**, 535–551.

Chappell, B. W. & White, A. J. R. (1992). I- and S-type granites in the Lachlan Fold Belt. In: Brown, P. E. & Chappell, B. W. (eds) *The Second Hutton Symposium on the Origin of Granites and Related Rocks, Geological Society of America, Special Papers* **272**, 1–26.

Chappell, B. W., White, J. R. & Wyborn, D. (1987). The importance of residual source material (restite) in granite petrogenesis. *Journal of Petrology* **28**, 1111–1138.

Clarke, D. B. & Carruzzo, S. (2007). Assimilation of country-rock ilmenite and rutile in the South Mountain Batholith, Nova Scotia, Canada. *Canadian Mineralogist* **45**, 31–42.

Clemens, J. D. (2006). Melting of the continental crust: fluid regimes, melting reactions, and source-rock fertility. In: Brown, M. & Rushmer, T. (eds) *Evolution and Differentiation of the Continental Crust*. Cambridge University Press, pp. 297–331.

Clemens, J. D., Helps, P. A. & Stevens, G. (2010). Chemical structure in granitic magmas—a signal from the source? *Earth and Environmental Science Transactions of the Royal Society of Edinburgh* **100**, 159–172.

Clemens, J. D., Stevens, G. & Farina, F. (2011). The enigmatic sources of I-type granites: the peritectic connexion. *Lithos* **126**, 174–181.

Conrad, W. K., Nicholls, I. A. & Wall, V. J. (1988). Water-saturated and -undersaturated melting of metaluminous and peraluminous crustal compositions at 10 kb: evidence for the origin of silicic magmas of the Taupo Volcanic Zone, New Zealand, and other occurrences. *Journal of Petrology* **29**, 765–803.

Daczko, N. R., Piazolo, S., Meek, U., Stuart, C. A., & Elliott, V. (2016). Hornblendite delineates zones of mass transfer through the lower crust. *Scientific Reports* **6**, 31369.

De Almeida, F. F. M. (1977). O Cráton São Francisco. *Brazilian Journal of Geology* **7**, 349–364.

Dorr, J. V. N. (1969). *Physiographic, stratigraphic and structural development of Quadrilatero Ferrifero, Minas Gerais, Brazil. USGS/DNPM, Professional Paper* **641-A**, 110 pp.

Drummond, M. S., Defant, M. J. & Kepezhinskas, P. K. (1996). Petrogenesis of slab-derived trondhjemite–tonalite–dacite/adakite magmas. In: Brown, M., Candela, P. A., Peck, D. L., Stephens, W. E., Walker, R. J. & Zen, E-an (eds) *The third Hutton Symposium on the Origin of Granites and Related Rocks, Geological Society of America, Special Papers* **315**, 205–215.

Erdmann, S., Jamieson, R. A. & MacDonald, M. A. (2009). Evaluating the origin of garnet, cordierite, and biotite in granitic rocks: A case study from the South Mountain Batholith, Nova Scotia. *Journal of Petrology* **50**, 1477–1503.

Farina, F., Stevens, G., Gerdes, A. & Frei, D. (2014). Small-scale Hf isotopic variability in the Peninsula pluton (South Africa): The processes that control inheritance of source ^{176}Hf/^{177}Hf diversity in S-type granites. *Contributions to Mineralogy and Petrology* **168**, 1–18.

Farina, F., Albert, C. & Lana, C. (2015). The Neoarchean transition between medium- and high-K granitoids: Clues from the Southern São Francisco Craton (Brazil). *Precambrian Research* **266**, 375–394.

Ganzhorn, A. C., Trap, P., Arbaret, L., Champallier, R., Fauconnier, J., Labrousse, L. & Prouteau, G. (2016). Impact of gneissic layering and localized incipient melting upon melt flow during experimental deformation of migmatites. *Journal of Structural Geology* **85**, 68–84.

Garcia-Arias, M. & Stevens, G. (2016). Phase equilibrium modelling of granite magma petrogenesis: A. An evaluation of the magma compositions produced by crystal entrainment in the source. *Lithos* **277**, 131–153.

Hasalová, P., Schulmann, K., Lexa, O., Štipská, P., Hrouda, F., Ulrich, S., Haloda, J. & Týcova, T. (2008a). Origin of migmatites by deformation-enhanced melt infiltration of orthogneiss: a new model based on quantitative microstructural analysis. *Journal of Metamorphic Geology* **26**, 29–53.

Hasalová, P., Štipská, P., Powell, R., Schulmann, K., Janoušek, V. & Lexa, O. (2008b). Transforming mylonitic metagranite by open-system interactions during melt flow. *Journal of Metamorphic Geology* **26**, 55–80.

Holland, T. & Blundy, J. (1994). Non-ideal interactions in calcic amphiboles and their bearing on amphibole–plagioclase thermometry. *Contributions to Mineralogy and Petrology* **116**, 433–447.

Hu, Z. P., Zhang, Y. S., Hu, R., Wang, J., Siebel, W. & Chen, F. (2016). Amphibole-bearing migmatite in North Dabie, eastern China: Water-fluxed melting of the orogenic crust. *Journal of Asian Earth Sciences* **125**, 100–116.

Johnston, A. D. & Wyllie, P. J. (1988). Constraints on the origin of Archean trondhjemites based on phase relationships of Nuk gneiss with H_2O at 15 kbar. *Contributions to Mineralogy and Petrology* **100**, 35–46.

Kemp, A. I. S., Hawkesworth, C. J., Foster, G. L., Paterson, B. A., Woodhead, J. D., Hergt, J. M., Gray, C. M. & Whitehouse, M. J. (2007). Magmatic and crustal differentiation history of granitic rocks from Hf–O isotopes in zircon. *Science* **315**, 980–983.

Lana, C., Alkimin, F. F., Armstrong, R., Scholz, R., Romano, R. & Nalini, H. A., Jr (2013). The ancestry and magmatic evolution of Archaean TTG rocks of the Quadrilátero Ferrífero province, southeast Brazil. *Precambrian Research* **231**, 157–173.

Lavaure, S. & Sawyer, E. W. (2011). Source of biotite in the Wuluma Pluton: Replacement of ferromagnesian phases and disaggregation of enclaves and schlieren. *Lithos* **125**, 757–780.

McDonough, W. F. & Sun, S. S. (1995). The composition of the Earth. *Chemical Geology* **120**, 223–253.

Montel, J. M. & Vielzeuf, D. (1997). Partial melting of metagreywackes, Part II. Compositions of minerals and melts. *Contributions to Mineralogy and Petrology* **128**, 176–196.

Noce, C. M., Machado, N. & Teixeira, W. (1998). U–Pb geochronology of gneisses and granitoids in the Quadrilátero Ferrífero (southern São Francisco craton): age constraints for Archean and Paleoproterozoic magmatism and metamorphism. *Brazilian Journal of Geology* **28**, 95–102.

Noce, C. M., Teixeira, W., Quéméneur, J. J., Martins, V. T. & Bolzachini, É. (2000). Isotopic signatures of Paleoproterozoic granitoids from the southern São Francisco Craton and implications for the evolution of the Transamazonian Orogeny. *Journal of South American Earth Sciences* **13**, 225–239.

Oliver, N. H. S., Valenta, R. K. & Wall, V. J. (1990). The effect of heterogeneous stress and strain on metamorphic fluid flow, Mary Kathleen, Australia, and a model for large-scale fluid circulation. *Journal of Metamorphic Geology* **8**, 311–331.

Oliveira, A. H. & Carneiro, M. (2001). Campo Belo Metamorphic Complex: tectonic evolution of an Archean sialic crust of the southern São Francisco Craton in Minas Gerais (Brazil). *Anais da Academia Brasileira de Ciências* **73**, 397–415.

Palin, R. M., White, R. W., Green, E. C., Diener, J. F., Powell, R., & Holland, T. J. (2016). High-grade metamorphism and partial melting of basic and intermediate rocks. *Journal of Metamorphic Geology* **34**, 871–892.

Patiño Douce, A. E. & Harris, N. (1998). Experimental constraints on Himalayan anatexis. *Journal of Petrology* **39**, 689–710.

Patiño Douce, A. E. & Johnston, A. D. (1991). Phase equilibria and melt productivity in the pelitic system: implications for the origin of peraluminous granitoids and aluminous granulites. *Contributions to Mineralogy and Petrology* **107**, 202–218.

Reichardt, H. & Weinberg, R. F. (2012). Hornblende chemistry in meta- and diatexites and its retention in the source of leucogranites: An example from the Karakoram Shear Zone, NW India. *Journal of Petrology* **53**, 1287–1318.

Reichardt, H., Weinberg, R. F., Andersson, U. B. & Fanning, C. M. (2010). Hybridization of granitic magmas in the source: the origin of the Karakoram Batholith, Ladakh, NW India. *Lithos* **116**, 249–272.

Romano, R., Lana, C., Alkimin, F. F., Stevens, G. & Armstrong, R. (2013). Stabilization of the southern portion of the Sao Francisco Craton, SE Brazil, through a long-lived period of potassic magmatism. *Precambrian Research* **224**, 143–159.

Rosenberg, C. L. & Handy, M. R. (2005). Experimental deformation of partially melted granite revisited: Implications for the continental crust. *Journal of Metamorphic Geology* **23**, 19–28.

Rutter, E. H. & Mecklenburg, J. (2006). The extraction of melt from crustal protoliths and the flow behaviour of partially molten crustal rocks: an experimental perspective. In: Brown, M. & Rushmer, T. (eds) *Evolution and Differentiation of the Continental Crust*. Cambridge University Press, pp. 385–430.

Sawyer, E. W. (1987). The role of partial melting and fractional crystallization in determining discordant migmatite leucosome compositions. *Journal of Petrology* **28**, 445–473.

Sawyer, E. W. (1996). Melt segregation and magma flow in migmatites: Implications for the generation of granite magmas. In: Brown, M., Candela, P. A., Peck, D. L., Stephens, W. E., Walker, R. J. & Zen, E-an (eds) *The third Hutton Symposium on the Origin of Granites and Related Rocks, Geological Society of America, Special Papers* **315**, 85–94.

Sawyer, E. W. (1998). Formation and evolution of granite magmas during crustal reworking: The significance of diatexites. *Journal of Petrology* **39**, 1147–1167.

Sawyer, E. W. (2008). *Atlas of Migmatites. Canadian Mineralogist, Special Publication* **9**, 371 pp.

Sawyer, E. W. (2014). The inception and growth of leucosomes: Microstructure at the start of melt segregation in migmatites. *Journal of Metamorphic Geology* **32**, 695–712.

Sawyer, E. W., Cesare, B. & Brown, M. (2011). When the continental crust melts. *Elements* **7**, 229–234.

Skjerlie, K. P., Patiño Douce, A. E. & Johnston, A. D. (1993). Fluid-absent melting of a layered crustal protolith: Implications for the generation of anatectic granites. *Contributions to Mineralogy and Petrology* **114**, 365–378.

Stevens, G., Villaros, A. & Moyen, J.-F. (2007). Selective peritectic garnet entrainment as the origin of geochemical diversity in S-type granites. *Geology* **35**, 9–12.

Stevenson, R. K., Henry, P. & Gariépy, C. (2009). Isotopic and geochemical evidence for differentiation and crustal contamination from granitoids of the Berens River Subprovince, Superior Province, Canada. *Precambrian Research* **168**, 123–133.

Stuart, C. A., Daczko, N. R. & Piazolo, S. (2017). Local partial melting of the lower crust triggered by hydration through melt–rock interaction: an example from Fiordland, New Zealand. *Journal of Metamorphic Geology* **35**, 213–230.

Taylor, J. & Stevens, G. (2010). Selective entrainment of peritectic garnet into S-type granitic magmas: evidence from Archaean mid-crustal anatectites. *Lithos* **120**, 277–292.

Teixeira, W. & Figueiredo, M. C. H. (1991). An outline of Early Proterozoic crustal evolution in the São Francisco craton, Brazil: A review. *Precambrian Research* **53**, 1–22.

Teixeira, W., Carneiro, M. A., Noce, C. M., Machado, N., Sato, K. & Taylor, P. N. (1996). Pb, Sr and Nd isotope constraints on the Archean evolution of the gneissic-granitoid in the southern São Francisco Craton, Brazil. *Precambrian Research* **78**, 151–164.

Teixeira, W., Cordani, U. G., Nutman, A. P. & Sato, K. (1998). Polyphase Archean evolution in the Campo Belo Metamorphic Complex, Southern São Francisco Craton, Brazil: SHRIMP U–Pb zircon evidence. *Journal of South America Earth Sciences* **11**, 279–289.

Teixeira, W., Ávila, C. A., Dussin, I. A., Neto, A. C., Bongiolo, E. M., Santos, J. O. & Barbosa, N. S. (2015). A juvenile accretion episode (2·35–2·32 Ga) in the Mineiro belt and its role to the Minas accretionary orogeny: Zircon U–Pb-Hf and geochemical evidences. *Precambrian Research* **256**, 148–169.

Tindle, A. G. & Pearce, J. A. (1981). Petrogenetic modelling of *in situ* fractional crystallization in the zoned Loch Doon pluton, Scotland. *Contributions to Mineralogy and Petrology* **78**, 196–207.

Vielzeuf, D., Clemens, J. D., Pin, C. & Moinet, E. (1990). Granites, granulites, and crustal differentiation. In: Vielzeuf, D. & Vidal, P. (eds) *Granulites and Crustal Evolution*. Kluwer Academic, pp. 59–85.

Villaros, A., Stevens, G., Moyen, J.-F. & Buick, I. S. (2009). The trace element compositions of S-type granites: Evidence for disequilibrium melting and accessory phase entrainment in the source. *Contributions to Mineralogy and Petrology* **158**, 543–561.

White, A. J. & Chappell, B. W. (1977). Ultrametamorphism and granitoid genesis. *Tectonophysics* **43**, 7–22.